

PRISM: A Non-Equilibrium, Multiphase Interstellar Medium Model for Radiation Hydrodynamics Simulations of Galaxies

Harley Katz,¹★ Shenghua Liu,¹ Taysun Kimm,² Martin P. Rey,¹ Eric P. Andersson,³ Alex J. Cameron,¹ Francisco Rodriguez-Montero,¹ Oscar Agertz,³ Julien Devriendt¹ and Adrianne Slyz¹

¹*Sub-department of Astrophysics, University of Oxford, Keble Road, Oxford OX1 3RH, United Kingdom*

²*Department of Astronomy, Yonsei University, 50 Yonsei-ro, Seodaemun-gu, Seoul 03722, Republic of Korea*

³*Department of Astronomy and Theoretical Physics, Lund Observatory, Box 43, SE-221 00 Lund, Sweden*

Accepted XXX. Received YYY; in original form ZZZ

ABSTRACT

We introduce the PRISM interstellar medium (ISM) model for thermochemistry and its implementation in the RAMSES-RTZ code. The model includes a non-equilibrium primordial, metal, and molecular chemistry network for 115 species coupled to on-the-fly multifrequency radiation transport. PRISM accurately accounts for the dominant ISM cooling and heating processes in the low-density regime (i.e. $\rho < 10^5 \text{ cm}^{-3}$), including photoheating, photoelectric heating, H₂ heating/cooling, cosmic-ray heating, H/He cooling, metal-line cooling, CO cooling, and dust cooling (recombination and gas-grain collisions). We validate the model by comparing 1D equilibrium simulations across six dex in metallicity to existing 1D ISM models in the literature. We apply PRISM to high-resolution (4.5 pc) isolated dwarf galaxy simulations that include state-of-the-art models for star formation and stellar feedback to take an inventory of which cooling and heating processes dominate each different gas phase of a galaxy and to understand the importance of non-equilibrium effects. We show that most of the ISM gas is either close to thermal equilibrium or exhibits a slight cooling instability, while from a chemical perspective, the non-equilibrium electron fraction is often more than three times higher or lower than the equilibrium value, which impacts cooling, heating, and observable emission lines. Electron enhancements are attributed to recombination lags while deficits are shown to be due to rapid cosmic-ray heating. The PRISM model and its coupling to RAMSES-RTZ is applicable to a wide variety of astrophysical scenarios, from cosmological simulations to isolated giant molecular clouds, and is particularly useful for understanding how changes to ISM physics impact observable quantities such as metallic emission lines.

Key words: ISM: general – ISM: evolution – galaxies: ISM – galaxies: astrochemistry – galaxies: evolution

1 INTRODUCTION

The physical state of the interstellar medium (ISM) of galaxies results from a rich set of interacting thermodynamic, radiative, and chemical processes (e.g. [Draine 2011](#)). Understanding these processes is of key importance for inferring the physical properties of galaxies (e.g. gas density, metallicity, ionization parameter) from various types of observations across cosmic time and for modelling galaxy formation from first principles.

In the low-redshift Universe, the ISM is predicted (e.g. [Field et al. 1969](#); [McKee & Ostriker 1977](#); [Draine 2011](#); [Kim & Ostriker 2017](#)) to be a multiphase medium (i.e. multiple thermally stable gas phases coexist at the same pressure). While the ISM was originally envisioned to be a two-phase medium ([Field et al. 1969](#)), composed of a cold neutral medium (CNM) and a warm medium that can be both neutral (WNM) or ionized (WIM), it was later realized that the inclusion of supernova (SN) feedback generates a three-phase medium ([Cox & Smith 1974](#); [McKee & Ostriker 1977](#)): a CNM, a WNM/WIM, and a hot ionized medium (HIM). The exact properties of these phases (e.g. volume filling factors, total mass, temperature, etc.) are

sensitive to the detailed balance of cooling and heating processes, which are themselves dependent on the chemical state and radiation field of the medium, as well as the star formation rate and feedback processes that inject additional energy and drive shocks/turbulence. These processes are well studied (both observationally and theoretically) for the ISM of the Milky Way (e.g. [Wolfire et al. 1995, 2003](#)) and theoretical models have provided additional insight into lower metallicity environments (e.g. [Omukai 2000](#); [Omukai et al. 2005](#); [Bialy & Sternberg 2019](#)).

Due to the coupling between the chemistry and thermodynamics, different chemical species trace different phases of the ISM. For example, because O I has the same ionisation potential as H I, [O I] 63 μ m observations primarily trace neutral gas while the [O II] λ 3727 nebular line traces H II regions. In principle, moving up the O ionization ladder will trace progressively hotter gas. A key open question is how to convert between the emission or absorption that we see and the underlying physical properties of the galaxy.

1D spectral synthesis codes (e.g. [Hjellming 1966](#); [Williams 1967](#); [Binette 1985](#); [Sutherland & Dopita 1993](#); [Ferland et al. 1998](#)) are commonly employed for this purpose. Grids of models can be constructed to infer global galactic properties ([Kewley et al. 2001](#); [Morisset et al. 2015](#)) as well as combined to infer the underlying distribu-

★ E-mail: harley.katz@physics.ox.ac.uk

tion of properties from a single set of spectral lines (e.g. [Lebouteiller & Ramambason 2022](#)). Some of the primary advantages of these models are that they are fast to execute computationally, which allows for the exploration of large regions of parameter space and the relevant spatial scales (e.g. the different ionization fronts) can be resolved. However, one of the disadvantages is that they, being 1D, cannot generally capture the complex and dynamic structure of the ISM along with all of the relevant, time-varying star formation and feedback.

For this reason, a complementary approach is to simulate the physics of the ISM using 3D models. Numerically modelling the ISM requires high spatial resolution to capture many of the important processes, on the scale of parsecs (e.g. [Kim & Ostriker 2017](#); [Peters et al. 2017](#)), which is beyond the reach of most large-scale cosmological simulations ([Vogelsberger et al. 2014](#); [Dubois et al. 2014](#); [Schaye et al. 2015](#)). 3D simulations of individual patches of the ISM can achieve the required spatial resolution and additionally model the complex interplay of star formation and feedback (e.g. [Walch et al. 2015](#); [Girichidis et al. 2016](#); [Kim & Ostriker 2017](#); [Iffrig & Hennebelle 2017](#); [Hill et al. 2018](#); [Kim et al. 2020](#)), but they miss out on physics from larger scales and must put in dynamics (e.g. shearing) by hand. Simulations of isolated galaxies that also model much of the relevant physics are also now becoming possible (e.g. [Kannan et al. 2020](#); [Gutcke et al. 2021](#); [Richings et al. 2022](#); [Andersson et al. 2022](#)) and capture both large-scale galaxy motions and fluctuations in the radiation field from far away star formation. Cosmological zoom simulations of individual dwarf galaxies can now reach the required resolutions for ISM physics (e.g. [Rey et al. 2019](#)) and are able to capture further important physics such as accretion, a realistic circumgalactic medium, and environmental effects. However, the modelling techniques and the included physics varies widely between these different simulations. Importantly, to date, most simulations do not include any form of non-equilibrium metal chemistry.

In metal-enriched environments, it is often the case that metallic species dominate the cooling rate (e.g. [Sutherland & Dopita 1993](#); [Wiersma et al. 2009](#)). Thus, if a species is out of equilibrium, it can not only impact the observable emission, but also the thermodynamics of the gas. For the particular use case of comparing with spectroscopic observations, capturing both the correct evolution of the metal chemistry and the temperature state of the ISM is paramount. However, solving a large chemical network within a 3D simulation can be very computationally expensive. It is therefore common to “post-process” numerical simulations with photoionization codes or chemical networks in order to measure the metal ionization states and their relevant emission after the simulation has been run (e.g. [Olsen et al. 2018](#); [Katz et al. 2019](#); [Lupi et al. 2020](#); [Gong et al. 2020](#); [Barrow et al. 2020](#); [Pallottini et al. 2022](#)). Simulations can also be run with substantially reduced chemical networks that target an atom or molecule of interest for a specific problem. One of the crucial assumptions that is often made when post-processing simulation outputs or when using a substantially reduced chemical network is that the atoms and molecules that are not followed self-consistently are in equilibrium. Depending on environment this assumption is not guaranteed to be true because the timescales of different physical processes (e.g. cooling and recombination) are not necessarily synchronized (e.g. [Kafatos 1973](#); [Gnat & Sternberg 2007](#)).

There are now numerous 3D numerical simulations that employ much larger chemical networks (e.g. [Glover & Clark 2012b](#); [Oppenheimer & Schaye 2013](#); [Richings et al. 2014](#); [Gray et al. 2015](#); [Oppenheimer et al. 2018](#); [Richings et al. 2022](#)). Due to the expense of solving these networks, few of these codes couple the chemistry to on-the-fly radiation hydrodynamics. However, within the same

galaxy, the photoionization and photoheating rates can vary by many orders of magnitude (e.g. [Rosdahl et al. 2015](#)), which can lead to strong local variations in ion abundances. Recently, [Richings et al. \(2022\)](#) applied the LEBRON method for approximate radiative transfer ([Hopkins et al. 2018](#)) and found order of magnitude variations in the H and H₂ abundances in particular regions of temperature-density phase-space and changes of up to a factor of two in various emission line luminosities when comparing equilibrium and non-equilibrium solutions. Similarly, [Katz \(2022\)](#) showed that common bright emission line luminosities (e.g. [O III] $\lambda 5007$, [O II] $\lambda 3727$) calculated with various post-processing methods can be an order of magnitude different from the non-equilibrium value.

In general, the impact of non-equilibrium physics on galaxy formation, especially that involving metal chemistry, remains relatively unexplored. This motivated the development of the RAMSES-RTZ code ([Katz 2022](#)), which leverages the computational efficiency of both the M1 radiative transfer scheme ([Levermore 1984](#); [Rosdahl et al. 2013](#)) and a fast ODE solver inspired by [Anninos et al. \(1997\)](#), as well as the parallel performance of the RAMSES code ([Teyssier 2002](#)) to accelerate the computation of non-equilibrium metal chemistry coupled to on-the-fly radiation hydrodynamics. The accelerations make it possible to run full cosmological simulations with such non-equilibrium physics. These first works with the RAMSES-RTZ code focused primarily on simulations of the early Universe and lower-metallicity environments ([Katz et al. 2022](#)). In this work, we introduce the PRISM model which computes the dominant heating and cooling processes in the ISM at both low and high metallicities. Our goal is to use high-resolution simulations of isolated galaxies to obtain a census of the relevant cooling and heating processes and to understand where and why ISM gas is in or out of thermal or chemical equilibrium. This framework presented here has already been employed to estimate the impact of temperature fluctuations on the mass-metallicity relation ([Cameron et al. 2022](#)) and will form a baseline for future cosmological, isolated galaxy, and giant molecular cloud simulations.

This paper is organized as follows. In Section 2 we describe the chemical network and the various cooling and heating processes included in the PRISM model, comparing to equilibrium predictions of 1D models of the ISM in the literature. In Section 3 we employ the PRISM model in high-resolution 3D simulations of two isolated dwarf galaxies and provide a census of the processes that contribute to cooling or heating the ISM and discuss the impact of non-equilibrium physics. Finally, in Sections 4 and 5, we highlight the model limitations and anticipated model developments and present our conclusions.

2 CHEMISTRY AND THERMODYNAMICS

In this work, we present a new model for ISM physics called “PRISM” that is implemented in the RAMSES-RTZ¹ code ([Katz 2022](#)). The model has many similar features to various 1D implementations of cooling and heating processes in the ISM ([Wolfire et al. 1995](#); [Koyama & Inutsuka 2000](#); [Wolfire et al. 2003](#); [Bialy & Sternberg 2019](#)). We describe the ingredients of our model below and compare with previous work in the literature to demonstrate that the model is behaving as expected. Our goal is to demonstrate that our 3D code can converge to the correct equilibrium solution, regardless of ISM conditions.

¹ RAMSES-RTZ is an extension of both the RAMSES ([Teyssier 2002](#)) and RAMSES-RT ([Rosdahl et al. 2013](#)) codes.

Group Name	E_{low} (eV)	E_{high} (eV)	Function
IR	0.1	1.0	Infrared radiation pressure
Opt.	1.0	5.6	Direct radiation pressure
FUV	5.6	11.2	Photoelectric heating, Mg I, Si I, S I, Fe I ionization
LW	11.2	13.6	H ₂ dissociation, C I ionization
EUV ₁	13.6	15.2	H I, N I, O I, Mg II ionization
EUV ₂	15.2	24.59	H ₂ , C II, Si II, S II, Fe II, Ne I ion- ization
EUV ₃	24.59	54.42	He I, O II, C III, N II, N III, Si III, Si IV, S III, S IV, Ne II, Fe III ion- ization
EUV ₄	54.42	∞	He II, O III+, N IV+, C IV+, Mg III+, S V+, Si V+, Fe IV+, Ne III+ ioniza- tion

Table 1. Properties of the radiation energy bins in the simulation. We list the photon group name, the lower and upper energies, and the main function. An ion is listed if its ionization potential falls within the energy range of the bin. Ions listed with a “+” symbol indicate that all higher ionization states of the element fall within the bin.

2.1 Chemistry

Our code can follow the formation and destruction of up to 115 chemical species. This includes the primordial species of H I, H II, He I, He II, He III, and e^- (6), all metallic ionization states of O, C, N, Fe, S, Si, Mg, and Ne (107), as well as H₂ and CO molecules (2). The species are fully coupled to on-the-fly radiation hydrodynamics via eight frequency bins (see Table 1) and to the thermodynamics of the gas via various cooling and heating processes described below.

As described in Katz (2022), the code accounts for photoionization assuming cross sections from Verner et al. (1996), collisional ionization using rates from Voronov (1997), radiative recombination and dielectronic recombination adopting rates from Badnell (2006) and Badnell et al. (2003), respectively, and charge exchange reactions following Kingdon & Ferland (1996). A few reaction rates deviate from the default references provided here and these unique cases are well described in Katz (2022). In addition to the above-mentioned processes, new for this work, we have also included recombination on dust grains (Weingartner & Draine 2001) as well as cosmic-ray ionization.

2.1.1 H₂ formation and destruction

H₂ formation and destruction follows the method presented in Katz et al. (2017) with minor modifications. We assume that H₂ forms via two channels: on dust grains, and through a primordial process that primarily² involves H⁺. The reaction rate for H₂ formation on dust (R_d) is a combination of that presented in Gnedin et al. (2009) and Bialy & Sternberg (2019). We set

$$R_d = 3.5 \times 10^{-17} f_{\text{dg}} C \sqrt{\frac{T}{100 \text{ K}}} \text{ [cm}^3 \text{ s}^{-1}\text{]}, \quad (1)$$

where R_d is empirically derived in Wolfire et al. (2008), f_{dg} is the dust-to-gas mass ratio normalized to that of the Milky Way (see below), C is a clumping factor that accounts for unresolved density

² Note that we ignore three-body formation of H₂ as this process primarily occurs at densities much higher than we intend to probe with the code (e.g. Turk et al. 2011).

structure below the grid scale³, and T is the gas temperature. The primary modification in this work compared to Katz et al. (2017) are the explicit dependence of the reaction rate on temperature. Furthermore we adopt a f_{dg} that does not linearly scale with metallicity.

As we do not follow the non-equilibrium abundance of H⁺, at every time step, we solve for the equilibrium abundance of H⁺ by combining Equations 1, 2, 5, 13, 14, and 15 listed in Table B1 of Glover et al. (2010), with destruction rates of H⁺ due to cosmic-rays and the local radiation field. The rates of H⁺ destruction due to cosmic-rays and the local radiation field, which is new for this work, are scaled according to those used in Heays et al. (2017).

Finally, we account for self-shielding of H₂ from the local radiation field following Gnedin et al. (2009).

2.1.2 CO formation and destruction

Due to the inaccessibility of direct H₂ observations in many astrophysics environments, CO is often used to probe molecular gas (e.g. Bolatto et al. 2013). CO is now readily observed at $z > 5$ in a variety of sources (e.g. Riechers et al. 2019). From a theoretical perspective, CO is expected to be an important coolant of the ISM in high-density gas (e.g. Neufeld et al. 1995) due to it being one of the most common diatomic molecules (Solomon & Klemperer 1972). For these reasons, we include a model for CO formation and destruction in our chemical network.

Our CO model is based on those presented in Nelson & Langer (1997) and Glover & Clark (2012a). The formation rate of CO follows:

$$\frac{dn_{\text{CO}}}{dt} = k_0 n_{\text{C}^+} n_{\text{H}_2} \beta - \Gamma_{\text{CO}} n_{\text{CO}}, \quad (2)$$

where n_{CO} is the CO number density, $k_0 = 5 \times 10^{-16}$ (Nelson & Langer 1997), n_{C^+} is the C⁺ number density⁴, n_{H_2} is the molecular hydrogen number density, and $\Gamma_{\text{CO}} = 2.43 \times 10^{-10} G_0 f_{\text{sh,CO}} + 4.62 \times 10^{-15} (\eta_{\text{cr}}/10^{-16})$ is the destruction rate of CO which is the combination of destruction due to the UV radiation field and cosmic-ray ionization rate (η_{cr}). We account for self-shielding ($f_{\text{sh,CO}}$) by modulating the destruction due to the local radiation field (G_0) by interpolating tables from Lee et al. (1996) for CO, H₂ and dust, and measuring the column densities locally. Destruction coefficients are adopted from Heays et al. (2017)⁵.

CO formation is primarily governed by radiative association reactions that form CH_x (e.g. CH, CH₂, etc.) molecules. Because we do not follow CH_x molecules in our network, this physics⁶ is encapsulated in the coefficient β in Equation 2.

$$\beta = \frac{k_1 x_{\text{O}}}{k_1 x_{\text{O}} + \Gamma_{\text{CH}_x}/n_{\text{H}}}, \quad (3)$$

where $k_1 = 5 \times 10^{-10}$, n_{H} is the number density of hydrogen nuclei, x_{O} is the oxygen abundance fraction, and $\Gamma_{\text{CH}_x} = 1.41 \times 10^{-10} G_0 + 8.88 \times 10^{-15} (\eta_{\text{cr}}/10^{-16})$, with destruction coefficients adopted from

³ This parameter is often tuned to match an observed atomic-to-molecular transition. For this work, we will always assume $C = 1$.

⁴ In Nelson & Langer (1997) they assume that all C is in the form of C⁺. Because our chemical model follows individual C ionization states, we have relaxed this assumption and use the true C⁺ number density in each cell.

⁵ Note that our CO destruction coefficient due to the local radiation field is slightly higher than that presented in Glover & Clark (2012a) due to a different choice of atomic data.

⁶ This refers to the initial radiative association reaction of C⁺ + H₂ → CH₂⁺ which then converts to CH_x via further reactions with H₂ and electrons.

Metal	Fe	O	N	Mg	Ne	Si	Ca	C	S
f_{gas}	0.01	0.73	0.6	0.16	1	0.1	0.003	0.5	1

Table 2. Gas-phase fractions of each metal at solar metallicity. We do not allow the metals to be depleted below these fractions. Values of one indicate that the metal is always in the gas phase and hence not included in the dust model.

Heays et al. (2017). Because we follow the fluxes of sub-ionizing radiation directly in the simulation, the radiative transfer algorithm in RAMSES-RTZ already accounts for the absorption of this radiation by dust. Hence we can neglect the explicit dependence of the destruction rates of CO and CH_x on the dust optical depth.

2.1.3 Metal abundances and production

For models where we define an initial metallicity, we assume solar metal abundance patterns following Grevesse et al. (2010) and scale up and down depending on metallicity. For solar oxygen abundance, we use $12 + \log_{10}(\text{O}/\text{H}) = 8.69$ and when referring to “metallicity”, we specifically refer to that measured from the oxygen abundance. In simulations that include stellar particles or star formation, we also allow for the production of metals on-the-fly. Our model combines yields from Population III and Population II stars, via core-collapse supernova, hypernova (Pop. III only), pair-instability supernova (Pop. III only), type-Ia supernova, and AGB winds (Portinari et al. 1998; Heger & Woosley 2002; Nomoto et al. 2006; Seitenzahl et al. 2013; Pignatari et al. 2016) following the model in Andersson et al. (2022). Further description of the model and how we sample the stellar initial mass function is presented in Katz et al. (2022).

2.1.4 Dust model

While we do not currently follow the creation and destruction of dust on-the-fly, we employ an effective model for dust that is used for heating and cooling, attenuating the radiation field, radiation pressure, and metal depletion. Following earlier work (Kimm et al. 2018), we assume that the dust-to-gas mass ratio scales with metallicity based on the empirical results of Rémy-Ruyer et al. (2014). More specifically, we adopt their $X_{\text{CO,Z}}$ model fitted with a broken power-law. To be consistent with Rémy-Ruyer et al. (2014), the dust composition is assumed to be that of the BARE-GR-S model of Zubko et al. (2004).

The combination of a dust-to-gas mass ratio and dust composition sets the dust cross section as a function of wavelength which is used for attenuating the radiation field and for radiation pressure, the mass of metals locked up in dust (depletion), and the PAH abundance, which is needed for recombination rates on dust as well as dust heating and cooling. Since the dust-to-gas mass ratio is defined based on the oxygen abundance and the dust composition is fixed, differential metal production in our simulations can sometimes lead to unphysical depletion values (i.e. more of a particular metal is expected to be depleted than is available in the gas cell). To avoid this issue, we place an upper limit on the fraction that each metal can be depleted which reflects their gas-phase fractions at solar metallicity. These minimum allowed gas-phase percentages can be found in Table 2 and are a combination of the depletion values from Dopita et al. (2000) and the fraction of a metal expected to be depleted at solar metallicity by combining the Grevesse et al. (2010) abundances with the BARE-GR-S dust composition. Note that our method does not explicitly conserve the total mass of each element due to the fixed dust composition and this will be remedied in future work where

we explicitly model dust production and destruction on-the-fly (Rodríguez Montero et al. *in prep*).

2.2 Heating & Cooling

The total rate of change of energy density (E) in each gas element is defined as

$$\dot{E} = \sum_k \sum_i^{\text{processes species}} n_i \Gamma_k - \sum_k \sum_i^{\text{processes species}} \sum_j^{\text{species}} n_i n_j \Lambda_k, \quad (4)$$

for different combinations of species i and j , where the total heating rate is the sum of heating (Γ) due to cosmic rays, photoheating, photoelectric heating, and H₂ formation and dissociation heating. The net cooling rate is the sum of cooling (Λ) from primordial species (and their ions) such as H, He, and H₂, metal line cooling such as fine-structure transitions of O I and C II, CO molecular cooling, and dust processes such as recombination or grain-gas collisional cooling. Below we discuss the details of how each of these quantities is implemented in the PRISM model.

2.2.1 Cosmic-ray heating

Due to their long mean-free paths, cosmic-ray (and X-ray) ionization is the primary mechanism that sets the electron fraction at high densities. Cosmic-rays are also expected to dominate the heating rates at low densities, where photoelectric heating becomes less efficient. Our implementation of cosmic-ray interactions with primordial species follows Bialy & Sternberg (2019) (see their Equations 37-39). We consider both primary and secondary ionizations and the amount of heating per ionization event is adopted from Dalgarno & McCray (1972); Draine (2011). Free electrons can also directly interact with cosmic-ray protons. We adopt a heating rate due to this interaction following Goldsmith et al. (1969); Bialy & Sternberg (2019).

In addition to primordial species, we consider cosmic-ray heating due to interactions with metals. Primary cosmic-ray ionization rates for metals are based on Richings et al. (2014), following the methods of Lotz (1967); Silk (1970); Langer (1978). For these ionizations, we adopt the same heating rates as for primordial species. Due to the low number densities of metals, this mechanism is generally unimportant. However, interactions between cosmic-rays and H₂ can induce a UV field (Gredel et al. 1987, 1989) that leads to orders of magnitude more photodestruction of molecules such as CO or photoionization of metals with low ionization potentials compared to the primary cosmic-ray ionization rate. Photoionization and destruction rates from this induced UV flux are adopted from Heays et al. (2017) and the corresponding photoheating rates are calculated by differencing the mean photon energy of the induced spectrum above the relevant ionization potential.

For our fiducial model, we adopt a primary cosmic-ray ionization rate of $10^{-16} \text{ s}^{-1} \text{ H}^{-1}$ (e.g. Indriolo & McCall 2012), which is uniform in every cell of the simulation.

2.2.2 Photoheating

When photons ionize an atom or a molecule, the excess energy of the photon above the ionization potential is converted into kinetic energy that heats the gas. Since our radiation field is discretized, we follow Equation A16 in Rosdahl et al. (2013). In principle, the average photon energy in each bin should only consider local sources around the gas cell of interest. However, for computational efficiency,

we assume that the average photon energy in each bin is a luminosity-weighted sum of all sources in the computational volume.

2.2.3 Photoelectric heating

Photoelectric heating is one of the dominant ISM heating processes at solar metallicity. Our implementation follows that presented in Kimm et al. 2017 (see Equations 25 and 26), which is based on Bakes & Tielens (1994); Wolfire et al. (1995, 2003). Because we assume a different dust model compared to Kimm et al. (2017), we have modified our original implementation in two ways. First, we scale the heating rate with an empirically calibrated dust-to-gas mass ratio as a function of metallicity (see above, Rémy-Ruyer et al. 2014). Second, the normalization of the heating rate is dependent on the number of C atoms locked up in polycyclic aromatic hydrocarbons (PAHs). Wolfire et al. (2003) assume this to be 22×10^{-6} per H atom (Tielens et al. 1999). However, for our adopted BARE-GR-S model from Zubko et al. (2004), the number of C atoms locked up in PAHs is 33×10^{-6} per H atom. Thus we increase the heating rate compared to Wolfire et al. (2003) by a factor of 1.5.

2.2.4 H_2 heating

We consider three mechanisms by which H_2 heats the gas: formation, dissociation, and pumping. When H_2 forms, a fraction of the binding energy is released into the gas in the form of heat. Following Sternberg & Dalgarno (1989); Röllig et al. (2006), we assume that 1/3 of the 4.5 eV binding energy is released as heat.

When H_2 is dissociated due to Lyman-Werner band photons, we assume that 0.4 eV is deposited as heat into the gas (Black & Dalgarno 1977). Only $\sim 15\%$ of Lyman-Werner band photons are expected to dissociate H_2 , while the other $\sim 85\%$ simply excite the molecule (e.g. Draine & Bertoldi 1996). If the molecule is collisionally de-excited, the Lyman-Werner band photon is converted into heat. Otherwise, it is radiated away. Our model for heating due to H_2 pumping follows Equations 44 – 48 in Baczynski et al. (2015) that combines the UV pumping rate of H_2 from Draine & Bertoldi (1996) with the energy released per UV pumping event from Burton et al. (1990).

We also consider photoionization of H_2 by photons with $E > 15.2$ eV, which we assume always leads to dissociation via recombinative-dissociation. As with all photoionization, the excess energy of the photon above the ionization potential of the molecule is converted into heat.

2.2.5 Primordial atomic cooling

At $T \gtrsim 8000$ K, transitions in primordial atomic species (i.e. H and He), in particular $Ly\alpha$, often dominate the total cooling rate. Our implementation is the same as presented in Appendix E3 of Rosdahl et al. (2013). This includes contributions from collisional ionization cooling (Cen 1992), radiative recombination cooling (Hui & Gnedin 1997), collisional excitation cooling (Cen 1992), Bremsstrahlung cooling (Osterbrock & Ferland 2006), Compton cooling/heating (Haiman et al. 1996), and dielectronic recombination cooling (Black 1981).

2.2.6 H_2 cooling

At low metallicity ($\lesssim 10^{-5} Z_\odot$), H_2 cooling is the dominant process that allows the gas to cool below $\sim 10^4$ K (e.g. Saslaw & Zipoy 1967; Yoneyama 1972; Lepp & Shull 1984). For H_2 cooling, we

adopt the fits to tabulated data presented in Galli & Palla 1998 (see their Appendix A). The cooling function follows the form presented in Hollenbach & McKee (1979), accounting for the change in cooling above and below the critical density.

2.2.7 Metal-line cooling

In metal-enriched gas, metal-line emission is often the dominant coolant of the ISM. Our method is identical to that presented in Katz (2022) and we briefly describe it here. At $T < 10^4$ K, metal-line cooling is dominated by fine-structure transitions. We analytically calculate the level populations for O I, O III, C I, C II, N II, Fe I, Fe II, Si I, Si II, S I, and Ne II, assuming either a two-level or three-level system where relevant. Furthermore, we include stimulated emission coefficients in our level-population calculation to account for the CMB radiation field. We have updated all collisional partner data for the following collision partners: H, H^+ , ortho and para H_2 , e^- , He, He^+ , and He^{++} to be consistent with CLOUDY (Ferland et al. 2017). At $T > 10^4$ K, the dominant collisional partner for metal-line emission is electrons. For this reason, we adopt tabulated values for ion-by-ion cooling rates from Oppenheimer & Schaye (2013). In order to smoothly interpolate between the two temperature regimes, we have adopted the method of Bovino et al. (2016). The metal cooling rate is defined as

$$\Lambda_Z = f_1(T)\Lambda_Z^{\text{tabulated}} + f_2(T)\Lambda_Z^{\text{fine-structure}}, \quad (5)$$

where

$$\begin{aligned} f_1(T) &= 0.5[\tanh(c_{\text{sm}}(T - 10^4)) + 1] \\ f_2(T) &= 0.5[\tanh(c_{\text{sm}}(10^4 - T)) + 1], \end{aligned} \quad (6)$$

which smoothly interpolates between the fine-structure and tabulated cooling at $T \sim 10^4$ K. To limit overlap, we have increased the c_{sm} parameter from 10^{-3} as was used in Bovino et al. (2016) to 5×10^{-3} .

Our model allows for a reduced chemical network where not all metal ionization states are self-consistently tracked. More specifically, for computational efficiency, the most highly ionized state followed by our code is often less than the total number of possible ionization states. In this case, the most highly ionized state that we follow represents the total amount of gas in that ionization state or higher. For example, if we only track O I–O VI in the code, O VI really represents the ionization states of O VI–O IX. To calculate cooling in the situation where not all ionization states are tracked, we assume collisional ionization equilibrium (CIE) for all untracked higher ionized states and use the ion-by-ion cooling tables of Oppenheimer & Schaye (2013). In our example, the distribution of O in O VI–O IX will be calculated in CIE. A similar method was adopted by Gray et al. (2015).

2.2.8 CO cooling

Rotational and vibrational excitations of CO can lead to radiative cooling. We model both processes following Koyama & Inutsuka 2000 (see their Equations A10 and A11). Rotational cooling in the optically thin limit is derived from McKee et al. (1982), while vibrational cooling rates are adopted from Hollenbach & McKee (1989).

2.2.9 Dust recombination cooling

Charged particles can stick to the surfaces of PAHs which leads to gas cooling (e.g. Draine & Sutin 1987; Bakes & Tielens 1994). We have implemented this cooling process following Wolfire et al. 2003 (see

their Equation 21). Similar to our discussion of photoelectric heating, the assumed PAH abundance in our dust model is 50% higher than that of [Wolfire et al. \(2003\)](#), so we proportionally scale the cooling rate by a factor of 1.5.

2.2.10 Grain-gas collisional cooling

When the gas temperature is greater than the dust temperature, collisional interactions can lead to gas cooling ([Hollenbach & McKee 1989](#)). Different sized grains are expected to exhibit different temperatures; however, modelling a self-consistent grain size distribution and its coupling to the radiative transfer and gas is beyond the scope of this work. For simplicity, we follow [Draine \(2011\)](#); [Bialy & Sternberg \(2019\)](#) and assume that the dust temperature $T_{\text{dust}} = 17.9 \text{ K } G_0^{1/6}$, where G_0 is the flux of the FUV radiation field normalized to a value of $1.6 \times 10^{-3} \text{ erg s}^{-1} \text{ cm}^{-2}$ ([Habing 1968](#)). We adopt a fixed grain size of 100 \AA . The cooling (or heating) rate is then calculated following Equation 2.15 in [Hollenbach & McKee \(1989\)](#), with a modification to account for the changing dust-to-gas-mass ratio with metallicity.

2.3 Model Validation

To validate our model, we initialize a grid of 512 gas cells that smoothly interpolate density between $10^{-3} - 10^5 \text{ cm}^{-3}$ in log-space. All cells have an initial temperature of 10^4 K and are in an entirely neutral and atomic state. For our fiducial model, we set $G_0 = 1$, $C = 1$, and $\eta_{\text{cr}} = 10^{-16} \text{ s}^{-1} \text{ H}^{-1}$. We run the simulation six times, varying the metallicity in the range $10^{-5} Z_{\odot} - Z_{\odot}$ in steps of 1 dex. The gas density is fixed throughout the calculation and all simulations are evolved until equilibrium is reached.

In Figure 1 we show the equilibrium temperature (top) and pressure (bottom) as a function of gas density for the simulations with different metallicities (different colours). We note a few important features. First, at $Z \gtrsim 10^{-3} Z_{\odot}$, the pressure curve exhibits a canonical ‘S’ shape, as first described by [Field et al. \(1969\)](#), where gas at different temperatures (and densities) can co-exist at the same pressure. This indicates that the ISM is multiphase. Similar to others (e.g. [Norman & Spaans 1997](#); [Bialy & Sternberg 2019](#)), we find that this behaviour weakens and the gas evolves to higher pressures as metallicity goes to zero. Below $10^{-5} Z_{\odot}$, the gas is no longer multiphase. The reason for this is easily observed in the top panel of Figure 1 where at low-metallicity, the strength of the thermal instability is significantly suppressed.

For comparison, we show the solar-metallicity temperature-density curves of [Koyama & Inutsuka \(2000\)](#), [Wolfire et al. \(2003\)](#), [Bialy & Sternberg \(2019\)](#), and [Kim et al. \(2022\)](#) as the dotted, dashed, and solid red lines, respectively in Figure 1. Our model is most similar to that of [Bialy & Sternberg \(2019\)](#) and indeed we find the two curves have the same general behaviour. Thermal instability is triggered at $\rho \gtrsim 1 \text{ cm}^{-3}$, primarily due to O I and C II cooling. This can be seen in Figure 2 where we show the heating and cooling rates for different processes as a function of density for three different metallicities. At high densities at solar metallicity, we see an increase in temperature (see Figure 1). This is driven by H_2 heating (see the top panel of Figure 2). Mild discrepancies between our curves and those of [Bialy &](#)

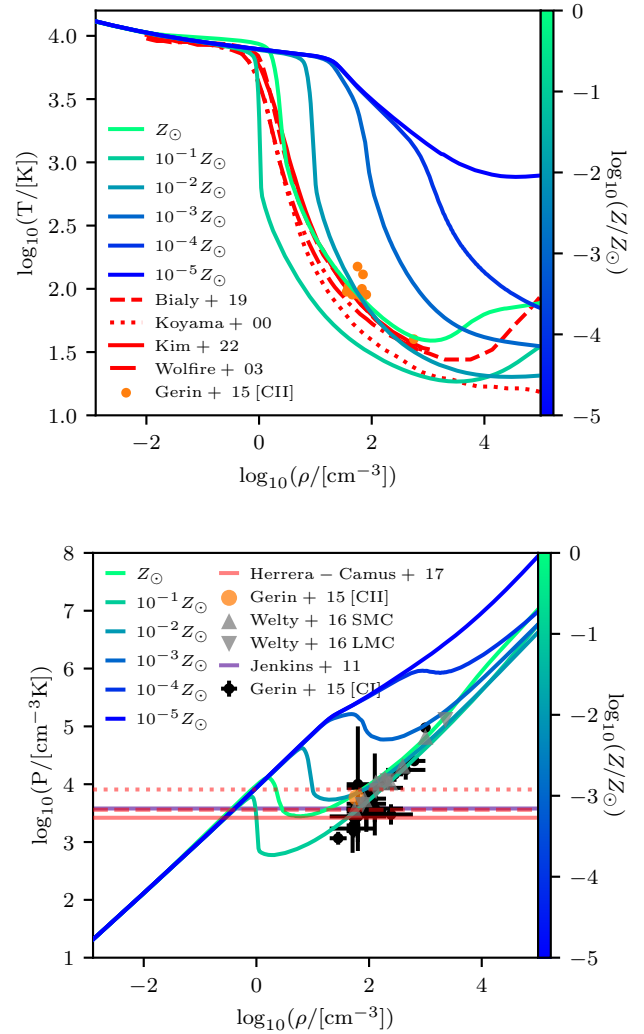


Figure 1. (Top) Equilibrium temperature-density relations as a function of metallicity. The dashed, dotted, dashed-dotted, and solid red lines show the results from [Bialy & Sternberg \(2019\)](#), [Koyama & Inutsuka \(2000\)](#), [Wolfire et al. \(2003\)](#), and [Kim et al. \(2022\)](#) respectively, at solar metallicity. Orange points represent [C II] observational constraints in the galactic plane from [Gerin et al. \(2015\)](#). (Bottom) Equilibrium pressure-density relations as a function of metallicity. We compare our results to the galactic plane pressure measurements from [Gerin et al. \(2015\)](#) using [C I] (black) or [C II] (orange) emission, from [Jenkins & Tripp \(2011\)](#) (purple), and those from [Herrera-Camus et al. \(2017\)](#) for different CNM fractions of 0.7, 0.5, and 0.3 as red dashed, solid, and dotted lines, respectively. LMC and SMC constraints from [Welty et al. \(2016\)](#) are shown as grey triangles.

[Sternberg \(2019\)](#) are likely due to differences in metal abundances⁷, dust depletions, and reaction and heating/cooling rates.

Our solar metallicity model is consistent with observational constraints of the pressure in the galactic plane. This includes data from [Herrera-Camus et al. \(2017\)](#) (assuming a CNM fraction of 0.3) and from [Gerin et al. \(2015\)](#), both their [C I] and [C II] observations. The

⁷ [Bialy & Sternberg \(2019\)](#) assume a solar O and C abundance of 5.4×10^{-4} and 3.0×10^{-4} , respectively, while [Koyama & Inutsuka \(2000\)](#) assume 4.6×10^{-4} and 3.0×10^{-4} . The fiducial abundances we adopt from [Grevesse et al. \(2010\)](#) are 4.9×10^{-4} and 2.69×10^{-4} for O and C, respectively.

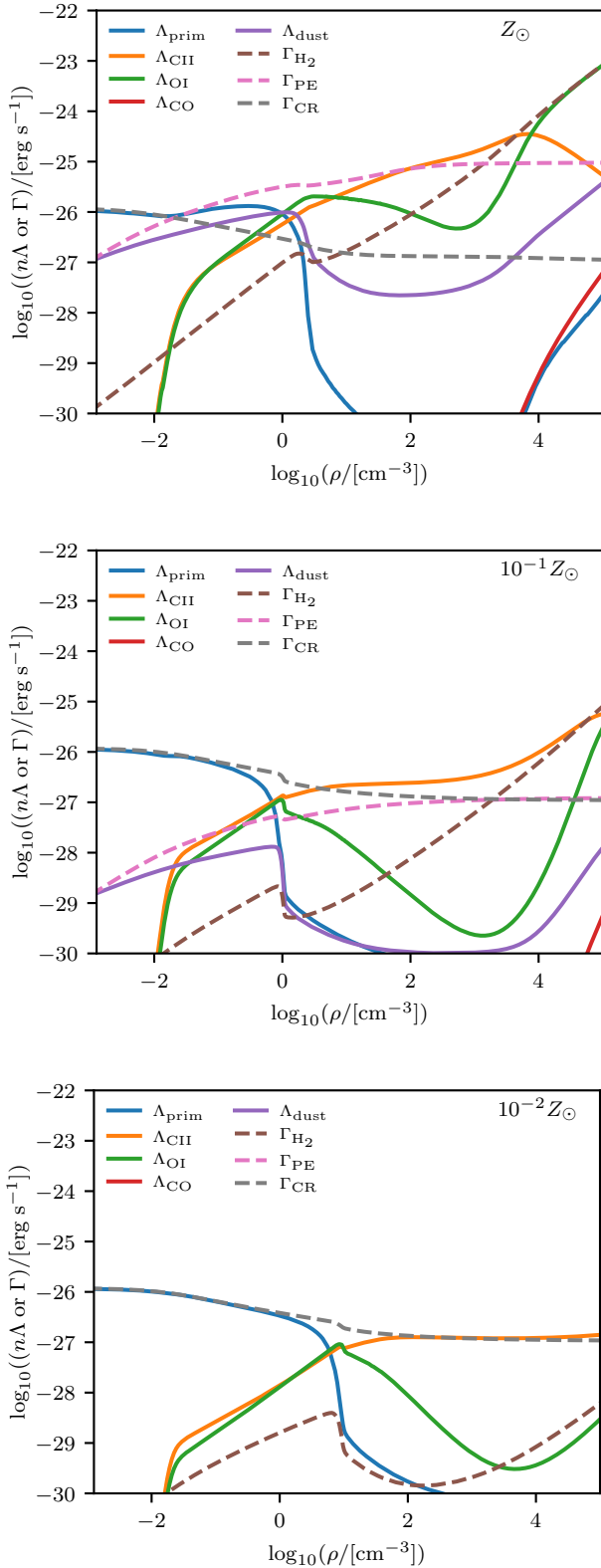


Figure 2. Equilibrium heating (dashed lines) and cooling (solid) rates for various processes as a function of gas density for three different metallicities as indicated on each panel. Different colours represent different processes including primordial cooling from H, He, and H₂ (blue), C II fine-structure cooling (orange), O II fine-structure cooling (green), CO molecular cooling (red), dust recombination and dust-gas collisional cooling (purple), H₂ formation and destruction heating (brown), photoelectric heating (pink), and cosmic-ray heating (gray).

clear amount of scatter in the observational data suggests that there is no single equilibrium curve that is fully representative. Modulating the abundances/depletion factors, cosmic ray ionization/heating rates, and photoelectric heating rates within the uncertainties for the galaxy can bring the pressure curve into agreement with any of this observational data (which itself is subject to modelling uncertainties).

Once the metallicity is decreased by a factor of ten, thermal instability occurs at lower densities compared to solar. This is because at this metallicity, the dust-to-gas mass ratio is lowered by more than a factor of ten, which both reduces the amount of depletion of metals, and reduces the impact of photoelectric heating (as described in Bialy & Sternberg 2019). The middle panel of Figure 2 shows the strength of the primary heating and cooling processes at $10^{-1} Z_{\odot}$ and for our model, cosmic-ray heating always dominates over photoelectric heating at this metallicity. The pressure curve for $10^{-1} Z_{\odot}$ is predicted to be lower than the solar metallicity case (see Figure 1). Interestingly, this prediction is in agreement with the thermal pressure constraints in the LMC and SMC from Welty et al. (2016), shown as grey triangles in Figure 1.

Moving to even lower metallicities, the thermal instability occurs at higher densities, until cooling is completely dominated by H₂ (between $10^{-4} Z_{\odot} - 10^{-5} Z_{\odot}$). There is a stark contrast between high- and low-metallicity in that at high metallicities, H₂ primarily acts to heat the gas while at low-metallicities, it is responsible for cooling (see e.g. Omukai 2000; Omukai et al. 2005). By this point, photoelectric heating is negligible and the only heating terms that matter in this test are those from cosmic-rays and H₂.

In Figure 3, we show the fraction of H that is in the form of H I, H II, and H₂ (top panel) as well as the fraction of C that is in the form of C I, C II, and CO (bottom panel). Due to the lack of ionizing radiation, the hydrogen ionization fractions are set by collisional ionization and cosmic-ray ionization. For this reason, most of the H is neutral. At high enough densities and metallicities, recombination of H II on dust grains becomes efficient and the solar metallicity curve for H II begins to deviate from the other metallicities at $\rho = 1 \text{ cm}^{-3}$. This curve even reaches the H II-floor of 10^{-6} which is set for solver stability (but has no impact on the thermodynamics of the cloud).

The H₂ fraction exhibits strong evolution with both density and metallicity. At high metallicities, H₂ formation is primarily driven by the dust-formation channel while at low metallicities, formation switches to the H⁺ channel. At densities of 10^5 cm^{-3} , the H₂ mass fraction saturates at $\sim 10\%$ at solar metallicity. Note that these simulations apply a uniform radiation field with no self-shielding. Our 3D code accounts for self-shielding and thus this test is not fully representative of what we might expect in a 3D simulation as column densities cannot be measured in these one-zone tests.

As described above, the addition of CO is one of the major updates for this work compared to our earlier chemical networks. The bottom panel of Figure 3 shows that even at high densities, CO remains subdominant compared to other forms of C. Apart from solar metallicity, the vast majority of C is in the form of C II. This is because the ionization potential of C is $< 13.6 \text{ eV}$ and it can thus be ionized by the interstellar radiation field. However, at solar metallicity, recombination on dust can become important and at $\rho \gtrsim 10^3 \text{ cm}^{-3}$, we find that C I dominates over C II. Since our CO model requires C II for formation, the rate of increase of CO slows down above these densities at solar metallicity. This is likely one of the reasons that we produce slightly less CO at high densities compared to Bialy & Sternberg (2019). Nevertheless, when self-shielding is included in 3D simulations, we expect significantly more CO to form (Glover et al. 2010; Glover & Clark 2012a).

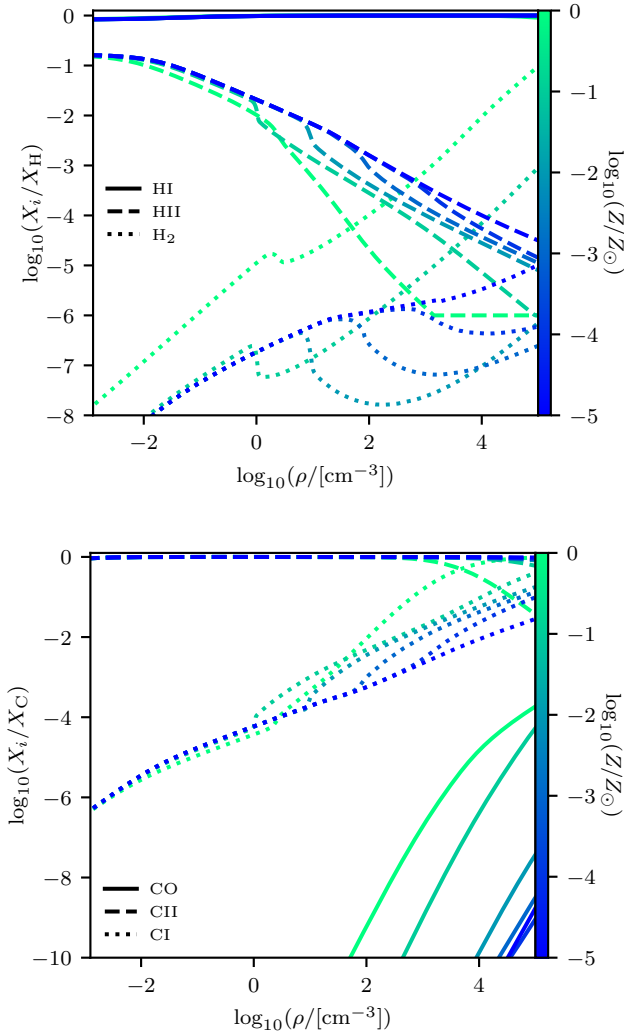


Figure 3. (Top) Equilibrium distribution of hydrogen in the form of H I (solid), H II (dashed), and H₂ (dotted) as a function of metallicity. (Bottom) Equilibrium distribution of carbon in the form of CO (solid), C II (dashed), and C I (dotted) as a function of metallicity.

The results shown in Figures 1, 2, and 3 are comparable to the 1D models presented in [Wolfire et al. \(1995\)](#); [Koyama & Inutsuka \(2000\)](#); [Wolfire et al. \(2003\)](#); [Bialy & Sternberg \(2019\)](#); [Kim et al. \(2022\)](#). The novel aspect of our model is that it is fully coupled to a 3D radiative hydrodynamics infrastructure that can be used to simulate realistic galaxies. The results above should provide confidence in our implemented ISM model and below, we exploit the 3D nature of our code to demonstrate the utility of our new framework.

3 NUMERICAL SIMULATIONS

As a first application of the PRISM model, we run high-resolution simulations of isolated dwarf galaxies to determine how the intuition gained from our 1D models translates to a 3D setting with full galaxy formation physics, where cooling, heating, and ionisation states are computed in non-equilibrium with on-the-fly radiative transfer, self-shielding, stellar feedback, metal production, and dynamics.

3.1 Methods

The simulations presented in this work are similar to those described in [Katz \(2022\)](#). Here, we provide a brief overview of the included physics and highlight the differences compared to our previous work.

The simulations follow the evolution of two isolated, rotating disk galaxies, named G8 and G9. The initial conditions for these galaxies are identical to those presented in [Rosdahl et al. 2015](#) (see their Table 1). G8 and G9 have halo virial masses of $10^{10} M_{\odot}$ and $10^{11} M_{\odot}$, and circular velocities of 30 km s^{-1} and 65 km s^{-1} , respectively. The disk gas masses are $3.5 \times 10^8 M_{\odot}$ and $3.5 \times 10^9 M_{\odot}$, both of which are embedded in a background gas density of 10^{-6} cm^{-3} . The initial central metallicity of G8 and G9 are $10^{-1} Z_{\odot}$ and $0.5 Z_{\odot}$ and we assume that the metallicity decreases with radius and height above the disk⁸. Initial chemical abundance ratios are scaled to the solar metallicity composition of [Grevesse et al. \(2010\)](#). To reduce computational expense, we employ a reduced chemical network, following eight ionization states of O, seven of N, six of C, Si, Mg, Fe, S, and Ne, as well as all ionization states of H, and He, in addition to the H₂ and CO molecules. The initial composition of the disk is assumed to be atomic and neutral, while outside the disk, all gas is assumed to be fully ionized.

The major difference between the simulations in [Katz \(2022\)](#) and those presented here are that we adopt the PRISM model for all ISM cooling and heating processes and use the updated chemistry as described in Section 2⁹. The simulations do not self-consistently follow cosmic-ray production or propagation so we employ a fixed cosmic-ray background ionization rate of $\eta_{\text{cr}} = 10^{-16} \text{ s}^{-1} \text{ H}^{-1}$. Unlike our 1D calculations, radiation hydrodynamics is self-consistently followed in eight energy bins (see Table 1). A reduced speed of light approximation is used ($c_{\text{sim}} = c/100$) to reduce computational expense. We consider two sources of radiation. The first is a UV background from [Haardt & Madau \(2012\)](#), which is spatially uniform throughout the computational volume. We apply a self-shielding approximation such that the intensity of the UV background is exponentially suppressed at $\rho > 10^{-2} \text{ H cm}^{-3}$ in H-ionizing radiation energy bins. The second source of radiation is star particles. Stars can form in the simulation following a thermo-turbulent star formation criteria ([Fedderrath & Klessen 2012](#); [Kimm et al. 2017](#)). Full details on the star formation recipe are presented in [Rosdahl et al. \(2018\)](#). Star particle masses are integer multiples of $1830 M_{\odot}$. Radiation is emitted from star particles based on their mass, age, and metallicity following a BPASS v2.2.1 SED ([Stanway & Eldridge 2018](#)). Feedback from stars is modelled for SNII, SNIa, and stellar winds ([Kimm et al. 2015](#); [Agertz et al. 2021](#)).

The second important difference between the simulations presented here compared to those in [Katz \(2022\)](#) is spatial resolution. Motivated by the work of [Kim & Ostriker \(2017\)](#) who demonstrated that many ISM properties converge in their model if the size of a gas cell is $\leq 8 \text{ pc}$, we allow the AMR grid in our simulations to refine up to a maximum resolution of 4.5 pc . Refinement in the simulation is triggered when the cell hosts eight times its initial mass in gas or to resolve the local Jeans length by four cells. This resolution is substantially improved compared to the 18 pc resolution used in [Katz](#)

⁸ In practice, we set $Z = Z_{\text{ini}} \times 10^{0.5-r/r_{\text{cut}}}$, where $r_{\text{cut}} = 5 \text{ kpc}$ for G8 and 11 kpc for G9.

⁹ Note that the simulations presented here use the old collisional rates from [Katz \(2022\)](#) for metal fine-structure cooling compared to the ones presented above and do not include the factor 1.5 boost for photoelectric heating and dust cooling due to the enhanced PAH abundance. The impact of these differences are discussed in Appendix A.

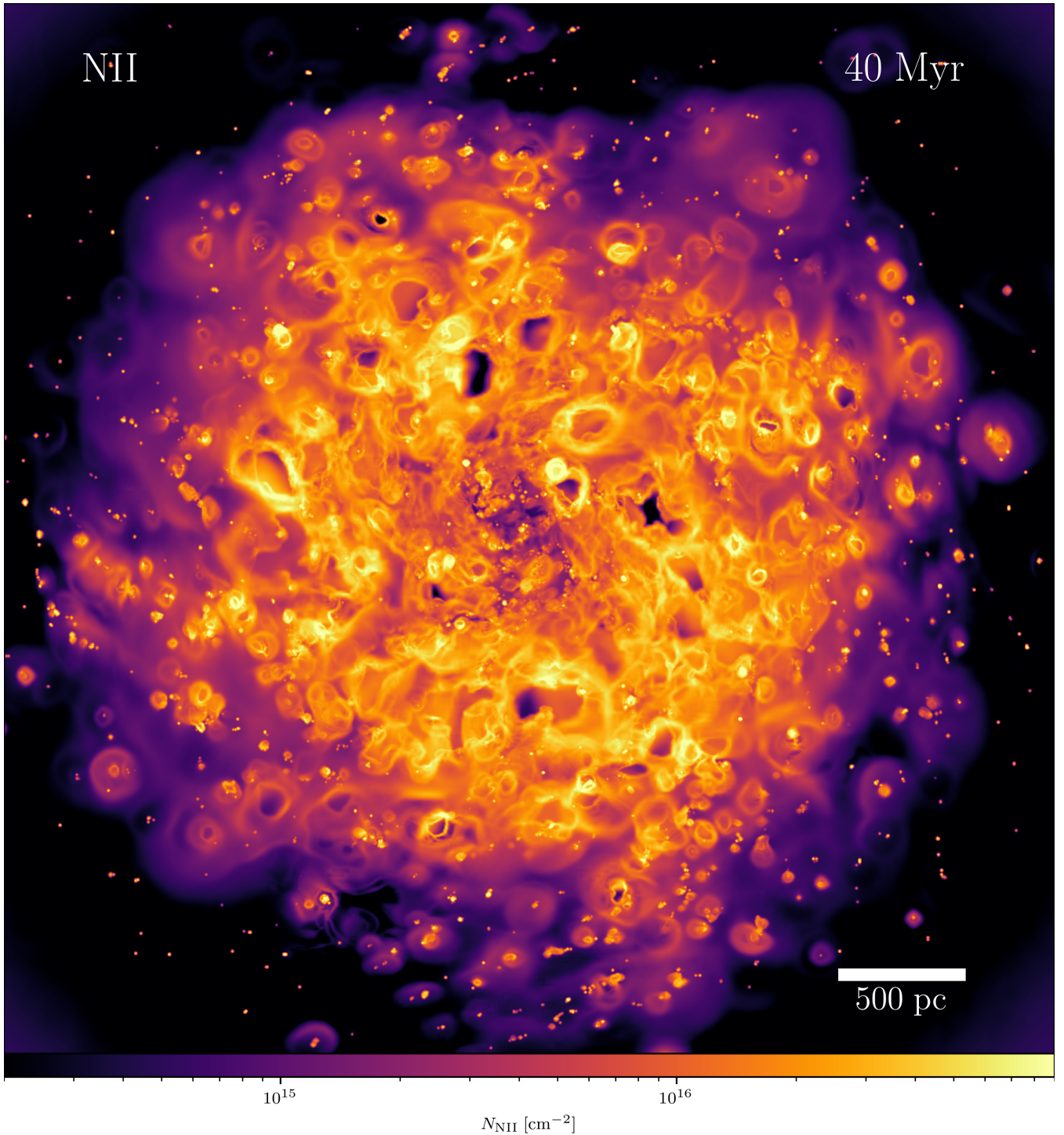


Figure 4. Column density map of N II in the central regions of G9 at 40 Myr. At this time, the star formation rate is $1.78 \text{ M}_{\odot} \text{ yr}^{-1}$. The ionization potential of N I is 14.5 eV so the map is tracing the H II regions around young stars as well as gas heated and enriched by supernova feedback. The diverse network of structure highlights the expected complexity and interactions between star-forming regions in real galaxies.

(2022). We exemplify this in Figure 4 where we show an N II column density of the central regions of G9 after 40 Myr, which is during the initial starburst phase of the galaxy. The N II is highly structured and follows young star-forming regions.

In what follows, we will focus on understanding how the results from the simulations differ from the 1D models.

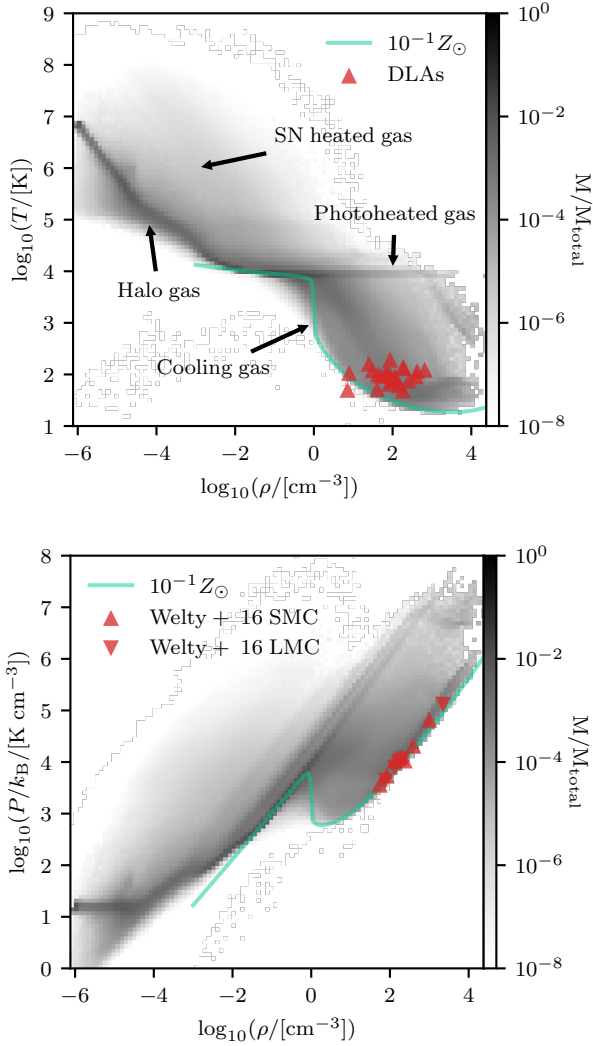


Figure 5. (Top) 2D mass-weighted histogram of temperature versus density for a stack of G8 snapshots from 150–400 Myr. We show density-temperature estimates for a sample of low- and high-redshift DLAs from Balashev et al. (2019); Klimentko & Balashev (2020) that are representative of low-metallicity systems. (Bottom) 2D mass-weighted histogram of pressure versus density for a stack of G8 snapshots from 150 – 400 Myr. For comparison, we show pressure measurements for LMC and SMC sight-lines from Welty et al. (2016) as red triangles. In both plots, the cyan line shows the location of our 1D equilibrium model at $10^{-1} Z_{\odot}$, the initial metallicity of the galaxy.

3.2 The density, pressure, and temperature distribution in the ISM

Due to the dynamic nature of the simulation, we expect the density, pressure, and temperature of the ISM to strongly deviate from the 1D models. In Figure 5 we show mass-weighted 2D histograms¹⁰ of temperature versus density (top) and pressure versus density (bottom)

¹⁰ We only consider gas with an oxygen mass fraction $> 10^{-8}$ which removes much of the pristine, artificial CGM in place in the initial conditions.

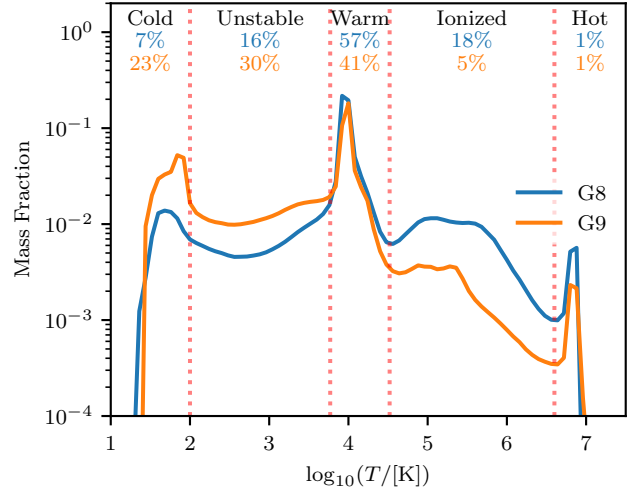


Figure 6. Mass fractions of gas as a function of temperature for a stack of G8 snapshots from 150–400 Myr (blue) and G9 snapshots from 150–200 Myr (orange). We differentiate phases of the ISM as cold ($T < 100$ K), unstable ($100 \text{ K} \leq T < 5,888 \text{ K}$), warm ($5,888 \text{ K} \leq T < 3.3 \times 10^4 \text{ K}$), ionized ($3.3 \times 10^4 \text{ K} \leq T < 4 \times 10^6 \text{ K}$), and hot ($T \geq 4 \times 10^6 \text{ K}$) based on natural breaks in the distribution function. The mass fraction of total gas in each phase is listed.

for a stack¹¹ of G8 snapshots from 150–400 Myr¹². At high densities and low temperatures, rather than a single track, we find that the gas distribution has bifurcated into two equilibrium trajectories (the same behaviour is seen for G9) and these are annotated as “cooling gas” and “photoheated gas”. The first extends towards low temperatures which represents the same equilibrium cooling curve that we find in the 1D models. There is considerably more scatter due to the fact that the metallicity varies between gas cells as does the sub-ionizing radiation field and the electron density. The second is gas that maintains a temperature of $\sim 10^4$ K even at high densities. For this second trajectory, photoionization heating and collisional heating from shocks (both of which are not included in the 1D models) can keep the gas in the warm phase. Between these two regimes, the gas is marginally unstable and we discuss this below.

The multiphase nature of the ISM is much more evident in the bottom panel of Figure 5. The two trajectories in temperature-density space are immediately visible in pressure-density space. From densities of $1 \text{ cm}^{-3} - 10^{4.5} \text{ cm}^{-3}$, the pressure spans nearly five orders of magnitude (at fixed density the range is closer to ~ 3 dex). For comparison, we show the observational estimates of gas pressure for SMC and LMC sight-lines from Welty et al. (2016) and they are in good agreement with our simulation.

Using these distributions, we can calculate how much mass is in each phase of the ISM. In Figure 6 we show the distribution function of gas mass as a function of temperature for the stack G8 snapshots (blue) and G9 snapshots between 150 – 200 Myr (orange). There are four natural breaks in the distribution that split the ISM into five phases, similar to those listed in Kim & Ostriker (2017). The demarcations are cold ($T < 100$ K), unstable ($100 \text{ K} \leq T < 5,888 \text{ K}$), warm

¹¹ We calculate the total mass of within each 2D bin across all snapshots and compute the PDF.

¹² We begin our analysis after 150 Myr to limit the impact of the disk settling from the initial conditions.

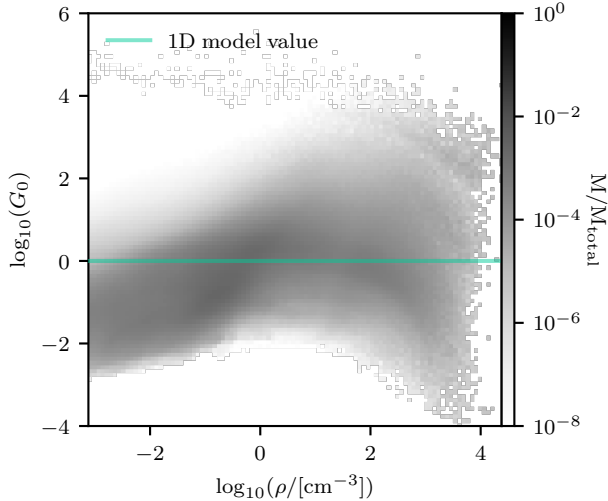


Figure 7. 2D mass-weighted histogram of the strength of the FUV radiation field (G_0) in units of $1.6 \times 10^{-3} \text{ erg s}^{-1} \text{ cm}^{-2}$ versus density for a stack of G8 snapshots from 150–400 Myr. In contrast to the 1D models (cyan), the simulated galaxy exhibits a large spread (up to eight orders of magnitude) in the strength of the FUV field at high densities which impacts the magnitude of photoelectric heating and the formation of molecules.

($5,888 \text{ K} \leq T < 3.3 \times 10^4 \text{ K}$), ionized ($3.3 \times 10^4 \text{ K} \leq T < 4 \times 10^6 \text{ K}$), and hot ($T \geq 4 \times 10^6 \text{ K}$). For G8, 7% of the gas is in a cold stable phase which should represent immediate fuel for star formation. A much larger fraction (57%) exists in warm phase near 10^4 K , consistent with Kim & Ostriker (2017). There is a significant amount of hotter ionized gas (18%) that is directly related to the strength of the feedback in our simulation. This phase is key for regulating star formation as it is a significant and relatively stable gas reservoir. G9 has a much more prominent cold and unstable phase compared to G8. The ionized phase has been reduced significantly. This is partially due to the higher metallicity of G9 which allows it to cool more efficiently. However, G9 has been run for a shorter period of time than G8 so the stellar feedback has not had as long to fully develop the ionized phase. If we restrict our G8 analysis to the same time period as G9, we find that the mass in the ionized phase is reduced by a factor of two. Because there is no accretion in our isolated setup, we expect the cold/unstable phases to be depleted as time progresses and the exact distribution of mass in cosmological simulations may be different due to gas accretion. Nevertheless, the key aspect is that we predict a well developed, multiphase ISM dominated by a warm phase, in contrast to similar simulations with different physics (e.g. Bieri et al. 2022).

3.3 The ISM radiation field

In our 1D models, we assumed a fixed value of G_0 , which not only sets the strength of various heating processes (e.g. photoelectric heating), but also sets the equilibrium abundances of molecules such as H_2 and CO as well as important ions such as C II. However in the simulation, the local value of G_0 in each gas cell is set by both the radiation emitted by stars (both locally and globally) and the dust and metal¹³ column density.

In Figure 7 we show a mass-weighted 2D histogram of G_0 versus

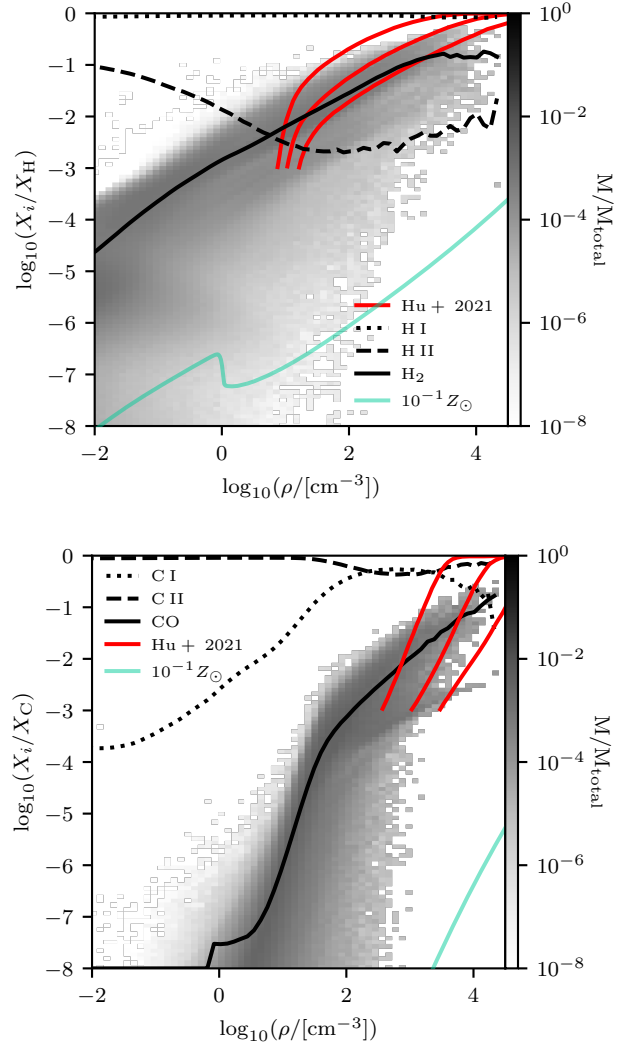


Figure 8. (Top) 2D mass-weighted histogram of the fraction of H in H_2 versus density for a stack of G8 snapshots from 150–400 Myr. The dashed, dotted, and solid lines show the mean fraction of H in the form of H I, H II, and H_2 , respectively as a function of density. (Bottom) 2D mass-weighted histogram of the fraction of C in CO versus density for a stack of G8 snapshots from 150 – 400 Myr. The various lines show the mean fraction of C in the form of C I, C II, and CO as a function of density as indicated in the legend. For comparison, we show the results from Hu et al. 2021 (red lines) for CO and H_2 at metallicities of Z_\odot , $0.3Z_\odot$, and $0.1Z_\odot$, from left to right, respectively. In both plots, the cyan line shows the location of our 1D equilibrium model at $10^{-1}Z_\odot$.

density for the stack of G8 snapshots. At very high densities of 10^4 cm^{-3} , the sub-ionizing radiation field varies by nearly eight orders of magnitude. This represents gas containing young stellar populations as well as gas that has recently cooled and condensed but has yet to form stars, and thus remains shielded. The behaviour of G9 is fundamentally similar, with even further enhanced scatter due to a higher star formation rate and higher gas densities/dust content. Towards lower densities, the scatter reduces and most of the gas has $G_0 < 1.0$, which is unsurprising given that the star formation rate of G8 is significantly lower than that of the Milky Way. The range of G_0 spanned in this histogram clearly demonstrates the necessity for on-the-fly radiative transfer.

¹³ Metallic ions such as C I, Fe I, etc. can absorb FUV radiation.

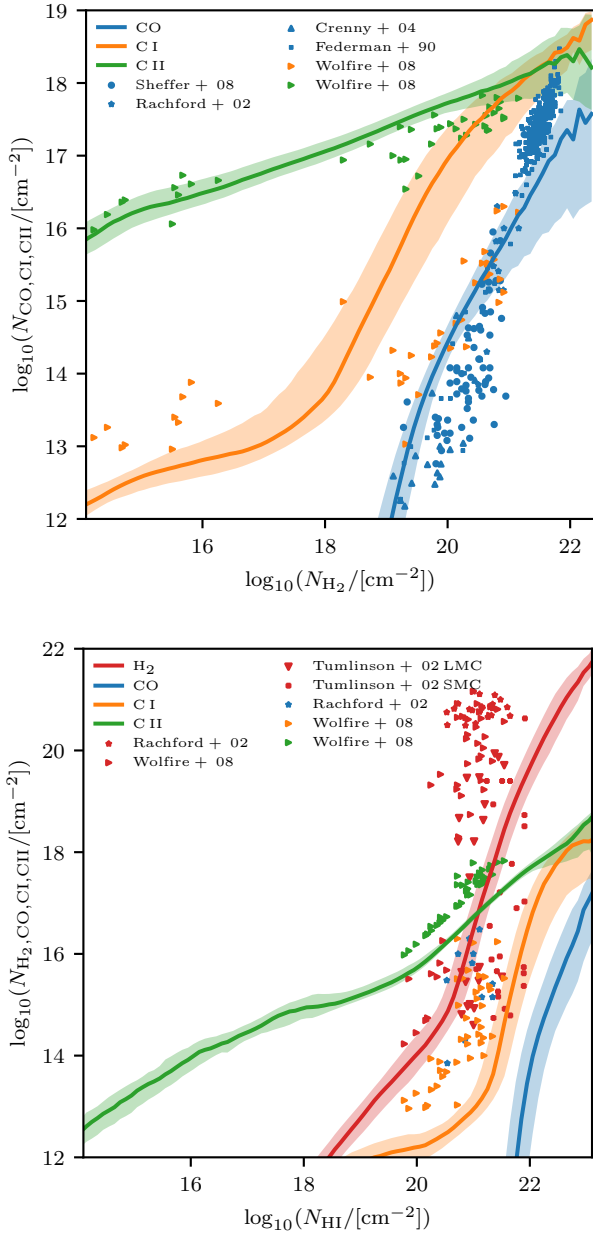


Figure 9. (Top) H₂ column density versus CO (blue), C I (orange), C II (green) column densities for a stack of G8 snapshots from 150–400 Myr. The solid line and shaded regions represent the median and 16–84 percentiles, respectively. (Bottom) H I column density versus H₂ (red), CO (blue), C I (orange), C II (green) column densities. For comparison, we show results from galactic sight lines from Federman et al. (1990); Rachford et al. (2002); Crenny & Federman (2004); Wolfire et al. (2008); Sheffer et al. (2008) and LMC and SMC sight lines from Tumlinson et al. (2002).

3.4 The molecular and neutral content of the ISM

Continuing with the molecular content, in Figure 8 we show 2D mass weighted histograms of the fraction of H in H₂ (top) and the fraction of C in CO (bottom) versus density for the stack of G8 snapshots. Compared to the 1D models, we form significantly more H₂ and CO. The two primary differences are the variable radiation field, which is often less than $G_0 = 1$ (as was assumed in the 1D models), but also the ability of the gas to self-shield. Due to the low metallicity

of G8, the H₂ fraction never saturates. However, at $\rho \sim 10^4 \text{ cm}^{-3}$, significantly more than 10% of H atoms are locked in H₂ molecules. In contrast, our solar metallicity 1D model predicted a value of $\sim 10\%$ while the $0.1Z_{\odot}$ model found a value between $10^{-5} - 10^{-4}$ (i.e. orders of magnitude below). We find similar behaviour in the fraction of C locked in CO atoms. At a density of 10^4 cm^{-3} , the 1D model predicted a value of $\sim 10^{-5}$. In contrast, 10% of the C is in the form of CO molecules at this density in the simulation.

Comparing the top and bottom panels of Figure 8, we find that while both the H₂ and CO fractions increase with density, H₂ has a much more gradual increase. At a density of 1 cm^{-3} the H₂ fraction is 0.1%. Although this is clearly subdominant, there is a substantial amount of gas in the simulation at this density. In contrast, there is essentially no CO at these same densities indicating that CO would not be a good tracer of diffuse H₂. A more detailed study of the relationship between H₂ and CO will be presented in future work.

Another noticeable difference between the 1D models and the simulation is the distribution of C I and C II. In the 1D models, there is no substantial amount of C I, except in the solar metallicity model at $\rho \gtrsim 10^3 \text{ cm}^{-3}$. There is an interesting regime in the simulation at $10^2 \text{ cm}^{-3} \lesssim \rho \lesssim 10^3 \text{ cm}^{-3}$ where C I dominates over C II. At these densities, the radiation field on average begins to weaken while the scatter increases (see Figure 7) and the contribution from recombination on dust allows for a phase where C I becomes important. Thus, we expect that fine-structure emission from C I will trace this unique phase for galaxies like G8. C II is the dominant phase of carbon at all other densities $> 10^{-2} \text{ cm}^{-3}$ in this simulated dwarf galaxy.

Despite the presence of a UV background and a local radiation field, the 1D model correctly predicts the H II fraction at a density of 10^{-2} cm^{-3} . In both the simulation and equilibrium model, the value at this density is 10%. Towards higher densities, the H II fraction drops off much more quickly in the 1D model while for the simulation, the mass-weighted mean H II fraction never drops below 0.1%. This is key because the residual electron fraction in the ISM is important for various cooling/heating processes as well as those that drive emission. At solar metallicity, the most abundant metal with an ionization potential $< 13.6 \text{ eV}$ is carbon with a number density (with respect to hydrogen) of 2.69×10^{-4} (excluding dust depletion). If the mean ionized fraction of H II is $\gtrsim 0.1\%$, this means that electrons from hydrogen atoms are a dominant contribution to the total electron fraction.

Understanding the atomic-to-molecular transition is key for modelling star formation (e.g. Gnedin et al. 2009; Christensen et al. 2012; Sternberg et al. 2014). Different choices of subgrid physics, atomic data, and chemical networks will impact at what densities and how fast this transition occurs. For comparison, we show the stratified box ISM simulation predictions of the H₂ and CO transition of Hu et al. (2021) in Figure 8 for three different metallicities. Their 3D simulations follow a non-equilibrium network for H₂ and are then post-processed with carbon chemistry. We note that there are quite strong differences in both the slopes of the relations as well as the densities at which the transition onsets. This is partially due to a different reaction network and a different model for FUV field adopted here compared to Hu et al. (2021). This comparison demonstrates the sensitivity of the transition to the chosen model.

Although our simulated galaxy is different from the Milky Way in terms of mass, metallicity, and kinematics, it is informative to compare the column densities of different ions and molecules to data from galactic sight lines where it has been measured (Federman et al. 1990; Rachford et al. 2002; Crenny & Federman 2004; Wolfire et al. 2008; Sheffer et al. 2008). In Figure 9 we compare the median H₂ column densities with the CO, C I, and C II column densities

(top) and the H I column densities with the H₂, CO, C I, and C II column densities (bottom). Interestingly, at low N_{H_2} , our N_{CII} is in very good agreement with Milky Way data but we find higher N_{CII} at high N_{H_2} compared to the Milky Way. In contrast, if we compare N_{HI} with N_{CII} , our simulations underpredict the N_{CII} values at high N_{HI} . Similarly we find lower N_{H_2} , N_{CI} , and N_{CO} at fixed N_{HI} compared to the Milky Way. We also find that G8 has higher N_{CI} at high N_{H_2} at $N_{\text{H}_2} > 10^{18} \text{ cm}^{-2}$ compared to the Milky Way. This could indicate that the recombination rates on dust used in PRISM are too strong or the radiation field is much weaker which allows more CI formation.

Compared to lower mass galaxies, G8 forms H₂ slightly more efficiently than the SMC but less efficiently than the LMC. This can be seen in the bottom panel of Figure 9 where we compare the N_{HI} vs. N_{H_2} curves to the observed data from Tumlinson et al. (2002).

The formation of H₂, C I, and CO are all linked to dust content as H₂ forms on dust, CO forms via H₂, and C I only becomes abundant when there is enough C enrichment, and either the dust content is high enough for recombination on dust or to shield the local FUV field. Thus the atomic-to-molecular transition in our model is likely to be sensitive to our choice of dust. The disagreement that we find when comparing various species column densities with N_{HI} in the Milky Way is very likely partially due to different metal and dust content of G8 compared to the Milky Way. We stress that this comparison is purely illustrative as the ISM in G8 exhibits very different conditions compared to the Milky Way.

3.5 Which processes cool and heat the ISM?

Constraining which processes cool and heat the ISM under a variety of conditions is of key importance for understanding how stars form. One of the primary advantages of following the individual ions and molecules fully coupled to the radiative transfer is that, in principle, our models for cooling and heating are much more self-consistent (e.g. the cooling matches the abundance and the ionization states) and accurate compared to traditionally adopted, tabulated cooling functions.

In Figure 10 we show the fractional contribution of different cooling (top) and heating (bottom) processes to the total cooling or heating rate as a function of density. The values are computed as the mass-weighted average for a stack of G8 snapshots from 150 – 400 Myr (solid lines) and similarly for G9 from 150 – 200 Myr (dashed lines). In general, at low densities ($< 0.5 \text{ cm}^{-3}$) cooling is dominated by primordial species (H, He, and H₂). Above this density threshold, fine-structure cooling from metal lines is the most important process. This result is very similar to the prediction from the 1D model.

It is often the case that O I and C II cooling are the most important metal ions; however, the contribution from other metal are non-negligible over a wide range in density. In our model, CO cooling is a subdominant process at all densities probed. At $\rho > 10^4 \text{ cm}^{-3}$, CO contributes up to 1% of the total cooling. This can increase in more massive, metal-enriched systems where CO may form more abundantly. Indeed we find that the contribution from CO cooling in G9 at high densities is much higher than in G8, peaking at $> 10\%$. Finally, dust processes (i.e. recombination cooling and gas-grain collisional cooling) become important at a density of $\sim 1 \text{ cm}^{-3}$, almost exactly where the thermal instability allows the gas to rapidly cool (see Figure 5). Similar to the 1D model, while dust processes are rarely the most important, they contribute at least 10% of the total cooling rate up to densities of $\sim 10 \text{ cm}^{-3}$. As we assume a relatively simplistic model for dust where the dust-to-gas-mass ratio is a fixed function of the gas-phase metallicity it is unclear how our findings

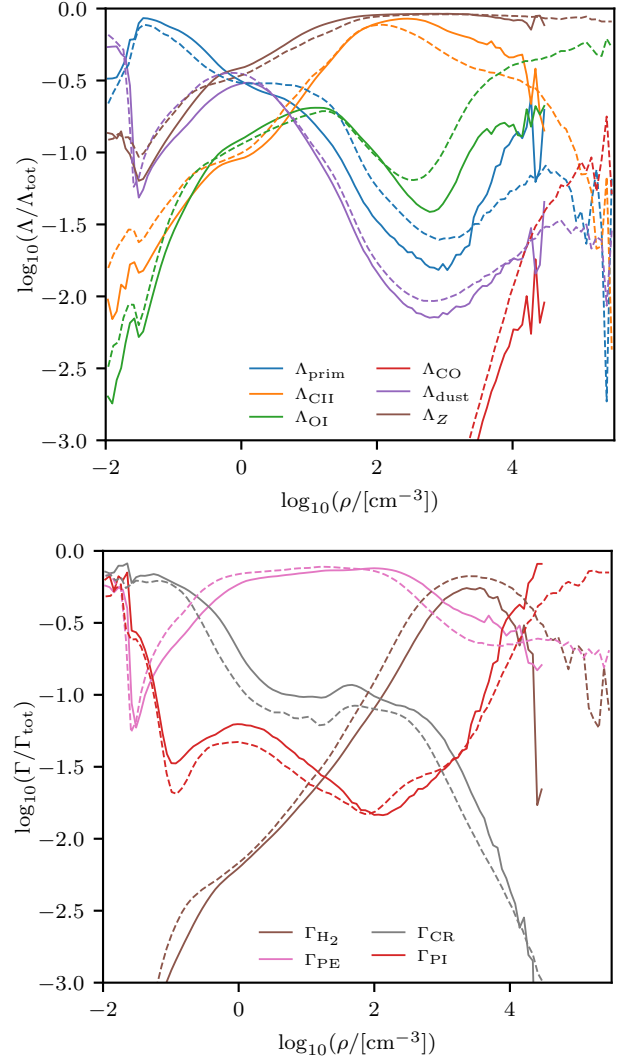


Figure 10. Fraction of the total cooling (top) or heating (bottom) contributed by various processes as a function of density as denoted in the legend. Solid and dashed lines represent a mass-weighted average for a stack of G8 snapshots from 150–400 Myr and G9 snapshots from 150–200 Myr, respectively.

will hold if dust is self-consistently formed and destroyed on-the-fly in the simulation. Future developments of the PRISM framework will allow for studying this in more detail.

In the 1D model, the transition between heating dominated by cosmic-rays versus the photoelectric effect occurred in the metallicity range $0.1Z_{\odot} - Z_{\odot}$. In the simulation, we find different behaviour. At $\rho \lesssim 0.3 \text{ cm}^{-3}$, cosmic-ray heating is generally the most important process (although there are situations where photoelectric heating and photoionization heating are also very important), as can be seen in the bottom panel of Figure 10. The crossover occurs at a similar density for both G8 and G9 but the exact density at which this transition occurs may change in simulations where cosmic-rays are produced and propagated on-the-fly. Transitioning to higher densities, photoelectric heating takes over up to nearly $\rho \sim 1000 \text{ cm}^{-3}$ for G8 and at a slightly lower value for G9. At higher densities, heating due to H₂ formation and destruction become very important. This was not seen in the 1D models where H₂ formed much less efficiently due to having a fixed G_0 and no shielding. At $\rho \gtrsim 7000 \text{ cm}^{-3}$, the

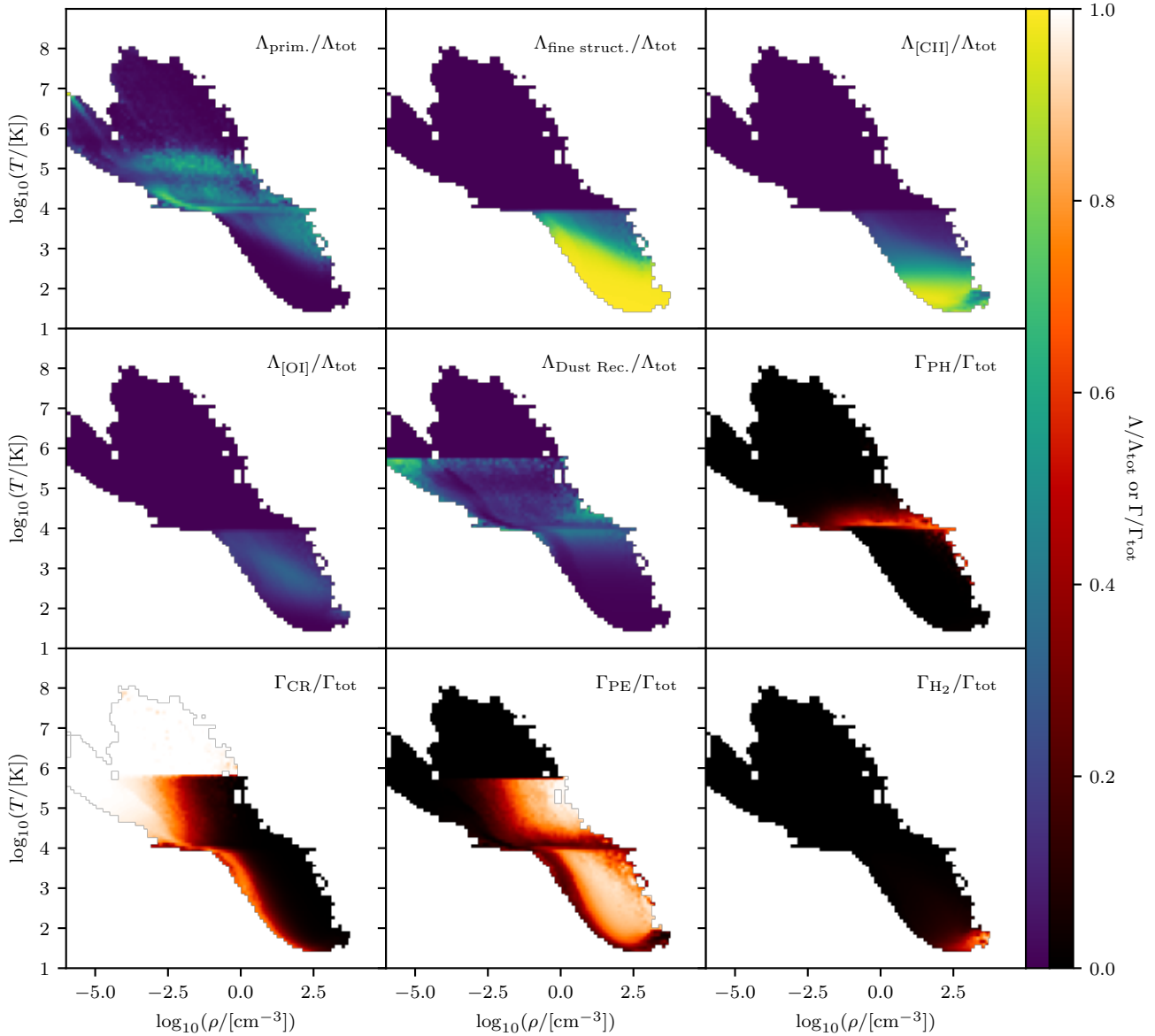


Figure 11. Density versus temperature diagrams for G8 at 400 Myr weighted by the fractional contribution of various cooling and heating processes to the total. Different gas phases of the galaxy are dominated by different cooling and heating processes. Pixels are only shown if they contain at least $1 M_{\odot}$ in gas. Note that H_2 cooling is included in the primordial cooling rate (top left panel). The sharp cutoff in the dust cooling and photoelectric heating are due to the assumption that all dust is destroyed at $T > 10^6$ K. Furthermore, the cutoff in fine-structure cooling at 10^4 K occurs because we switch from calculating the contribution from different ions individually assuming various collisional partners to tabulated rates assuming electrons dominate collisions.

gas is mostly residing near star-forming regions and photoionization heating rapidly dominates the total heating rate.

While Figure 10 highlights which cooling and heating process dominates for all mass at a given density, it is also important to recognize that variations also occur with temperature and spatially throughout the galaxy. In Figure 11 we show density-temperature phase-space diagrams for G8 at 400 Myr¹⁴ highlighted by the mass-weighted contribution of various cooling or heating rates to the total value. While fine-structure cooling from metals is the most important

cooling process at high densities, the contribution from primordial species is also highly significant in the warm, high-density gas. However, the gas is thermally unstable in these regions and thus cannot persist in this state for long. Hence, there is only a small amount of gas at high densities and high temperatures (see Figure 5).

Comparing the various heating processes, photoheating dominates a thin strip of gas at $T \sim 10^4$ K as well as the highest density and highest temperature gas. There is clear separation between where cosmic-ray, photoelectric, and H_2 heating are most important. Photoelectric and cosmic-ray heating both operate at all densities and temperatures, but cosmic-ray heating is more important at the lowest densities at fixed temperature, while the opposite is true for photo-

¹⁴ We verified that this snapshot is representative of other points in time in the simulation.

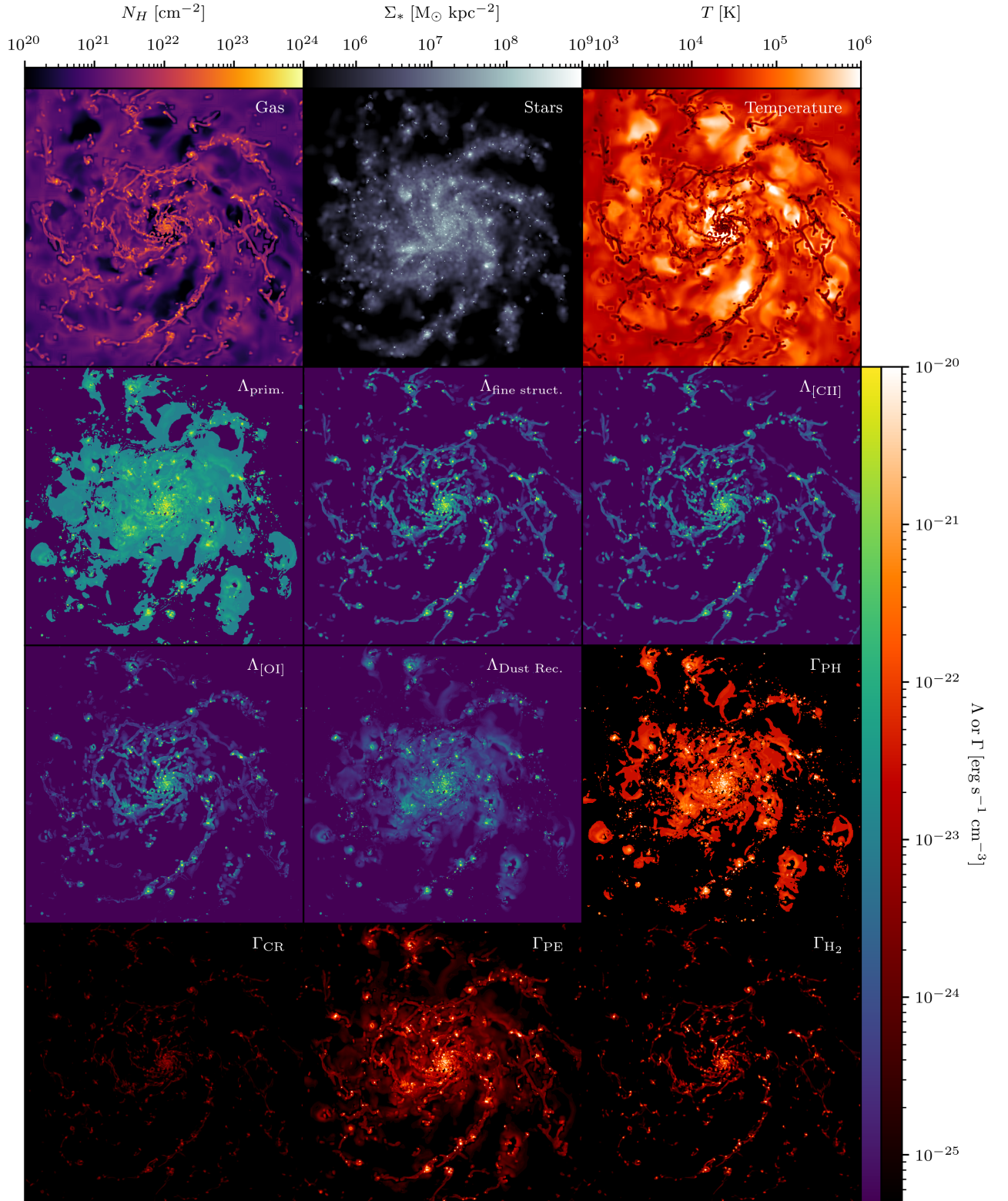


Figure 12. Maps of the total gas column density, stellar surface mass density, gas temperature (density-weighted along the line of sight), and various cooling and heating rates for different processes (density-weighted along the line of sight) for a representative snapshot of G9 at 161 Myr. The width of each image is 6.9 kpc.

electric heating. H_2 heating is only relevant at the highest densities and lowest temperatures where it forms most efficiently.

We note two particular features in Figure 11. The metal fine-structure contribution appears to become negligible above 10^4 K and heating and cooling associated with dust goes to zero above 10^6 K. In practice, we compute metal cooling at all temperatures; however, at $T \gtrsim 10^4$ K, metal cooling is dominated by collisional processes with electrons, while at lower temperatures other collisional partners matter. Here we show only the contribution at $T < 10^4$ K¹⁵. Furthermore, in our simplistic dust model, we assume that dust cannot exist at $T > 10^6$ K.

We also emphasize that here we only show heating or cooling processes that are explicitly calculated in our ISM model. Processes such as the PdV (adiabatic cooling/heating) work from SN explosions, shock heating, and gravitational compression heating, while calculated in the code, are not counted in the total cooling or heating rates shown. This is because these processes are operator split from the cooling and heating in PRISM and occur in the internal energy update when solving the Euler equations. Nevertheless, their importance should not be understated as they are key for driving gas to very high temperatures.

To conclude our analysis on which processes heat and cool the ISM, we show in Figure 12 density-weighted maps of various cooling and heating rates for G9 at 168 Myr¹⁶. For comparison, we also show maps of the total gas column density, stellar surface mass density, and gas temperature. Beginning with cooling, fine-structure metal-line cooling is primarily concentrated in the dense gas filaments. Cooling from primordial species, in contrast, extends into the much more diffuse gas between filaments. Dust recombination cooling is more concentrated around star-forming regions that are actively being metal enriched.

Continuing with heating processes, photoheating is patchy and traces the youngest star-forming regions. In some locations it is very concentrated around young stars when the nebula is ionization-bounded. However when stars are located in density-bounded gas clouds, the escape fraction from the birth cloud is high and photoheating can extend well beyond the star-forming region. Unsurprisingly, H_2 heating traces the densest gas filaments and is much more concentrated than, for example, [C II] or [O I] cooling. This has important implications for how well fine-structure emission from either of these two metals trace H_2 . Cosmic-ray heating is clearly the weakest of all processes shown so it is difficult to visually assess its importance in comparison to, e.g. photoelectric heating. This is primarily because it is most important in diffuse gas which, in general, has a low heating rate compared to other regions in the galaxy.

In summary, one of the primary advantages of the PRISM model is being able to take a census, fully in non-equilibrium, of where each cooling and heating process is regulating the thermodynamics of the ISM. It is clear that the contribution of each process is more complex in a dynamic 3D system than the 1D equilibrium models suggest. Below we will continue by assessing the importance of calculating cooling and heating in non-equilibrium.

3.6 When do non-equilibrium effects matter in the ISM?

One of the primary advantages of the coupling between the PRISM model and RAMSES-RTZ is that we can explore the impact of non-

equilibrium effects on the properties of the ISM. If the gas is significantly out of equilibrium, the 1D models will not be able to make robust predictions for ISM properties and observational signatures, which may bias our understanding of galaxy formation physics. In this Section, we identify where the gas is in and out of equilibrium and why.

3.6.1 Thermal Disequilibrium

We begin by analyzing where the gas is in and out of thermal equilibrium. In the top panel of Figure 13 we show the log ratio of total cooling to heating rate for G8 at 400 Myr. White regions represent where the gas is close to thermal equilibrium whereas blue and red regions indicate where cooling or heating dominate, respectively. There is a thin white band that extends from $T \sim 10^8$ K all the way down to $T \lesssim 10^4$ K where it bifurcates. The stronger branch extending towards lower temperatures follows the standard equilibrium cooling curve that one would obtain from collisional ionization equilibrium. This is similar to the cooling curves shown in Figure 1. The horizontal branch includes a photoheating contribution from star particles that maintains the ionization state and high temperature. These trajectories are exactly the same as those seen in the mass-weighted temperature-density diagram (Figure 5).

In general, the dense ISM is either very close to thermal equilibrium or has a slightly higher cooling than heating rate, indicative of a cooling instability. There are a few red pixels at high densities, which are regions around young star particles where photoheating is actively heating the gas. The lowest density regions of the ISM at $T < 10^4$ K are also red, partially from the impact of cosmic-ray heating. According to our model, the gas with the highest cooling to heating ratio is that at $T > 10^4$ K which primarily resides outside of the disk (although there is a warm and hot component of the disk as well). This is the gas that has been recently heated by SN feedback and driven out of the galaxy in a wind. Thermal instability in galactic winds within the context of our model is further studied in Rey et al. *in prep.*

One of the important consequences of the cooling instability is that it can lead to gas fragmentation on the scale of the cooling length (e.g. McCourt et al. 2018; Sparre et al. 2019; Mandelker et al. 2021), defined as $L_{\text{cool}} = c_s t_{\text{cool}}$, with c_s being the sound speed and t_{cool} being the cooling timescale. Following this line of reasoning, we can estimate what length scale we need to resolve in the simulation in order to capture this fragmentation (see also Smith et al. 2017). In the middle panel of Figure 13 we show the mass-weighted cooling length as a function of density and temperature for thermally unstable, cooling gas for G8 at 400 Myr. The densest regions of the ISM that are actively cooling have cooling lengths $\ll 1$ pc, far below the resolution scale of our simulation. Many of these same cells also have a Jeans' length below the resolution limit of the simulation (see the bottom panel of Figure 13). It is important to consider that 58% of the gas by mass is in thermal equilibrium or actively heating; however, among the cooling gas, 33% by mass has a cooling length smaller than the finest resolution element in our simulation. Although unsurprising, this indicates that the simulation is far away from structural convergence¹⁷ (see also Hummels et al. 2019; Peebles et al. 2019 for a similar discussion in the CGM). In other words, there could be structure below the resolution scale of

¹⁵ The two regimes are separated in the code as the former can easily be tabulated.

¹⁶ The results are similar for G8.

¹⁷ We note that this analysis does not account for non-thermal pressure support, such as that from turbulence, so the exact details of the fragmentation are subject to additional physics beyond a cooling or Jeans' instability.

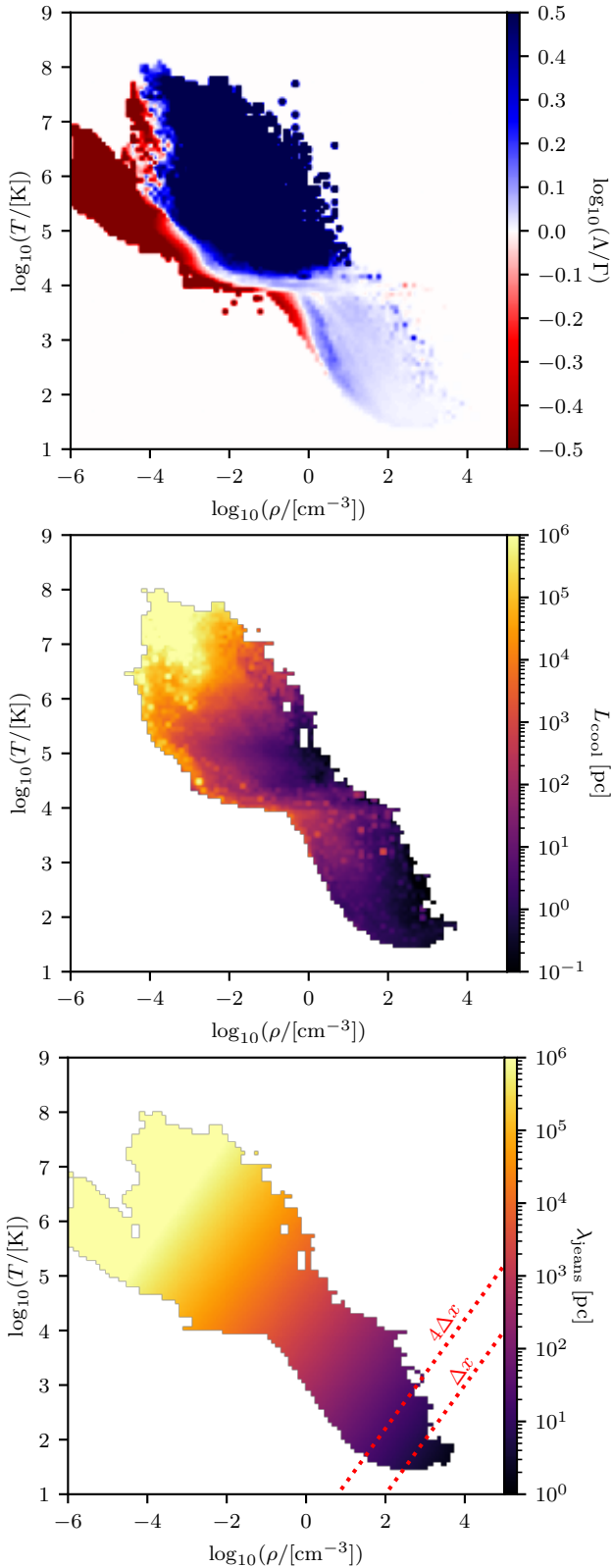


Figure 13. (Top) Logarithm of the ratio between the mass-weighted cooling and heating rates for G8 at 400 Myr as a function of temperature and density. Blue and red regions demonstrate where cooling or heating dominate, respectively, while white regions are in thermal equilibrium. (Middle) Mass-weighted cooling length for thermally unstable, cooling gas in G8 at 400 Myr as a function of temperature and density. (Bottom) Jeans length (λ_{jeans}) for gas cells in G8 at 400 Myr. The dotted red lines show contours of constant λ_{jeans} at the maximum resolution and four times the maximum resolution in our simulation.

the simulation that is important for chemistry, heating, cooling, and various other physical processes. Therefore, future versions of PRISM may require subgrid modelling for the density structure below the scale of the smallest resolution element to converge predictions with increasing resolution (e.g. Liu et al. 2022; Buck et al. 2022).

3.6.2 Chemical Disequilibrium

It is possible that the gas can be close to thermal equilibrium while being out of chemical (or ionization) equilibrium. It is well established that in the ISM, cooling timescales can be faster than recombination timescales, which leads to an ionization lag, where the gas is over-ionized compared to equilibrium (e.g. Kafatos 1973; Gnat & Sternberg 2007; Oppenheimer & Schaye 2013; Vasiliev 2013). Alternatively, if the heating timescale is faster than the ionization timescale, the gas may be under-ionized compared to equilibrium (e.g. Klessen & Glover 2016). Such an effect can be realized near shocks. In this Section, we discuss where the gas is out of chemical equilibrium and focus particularly on the electron fraction as it controls a substantial amount of heating and cooling processes as well as line emission from the galaxy.

To calculate whether a gas cell is in chemical equilibrium, we restart G8 from all snapshots between 175 – 250 Myr, fixing the temperature and radiation field, and evolve the simulation until chemical equilibrium is reached. In Figure 14 we show a 2D histogram of density versus temperature coloured by the log ratio of non-equilibrium to equilibrium mass-weighted electron fraction for a stack of all snapshots in this time period. Gas is only shown if it has an electron fraction $> 0.1\%$ in either the equilibrium or non-equilibrium output. In certain cases, the non-equilibrium electron fraction is more than three times the equilibrium value. Similarly high ratios were observed in Richings & Schaye (2016). We believe that the origin of this behaviour is due to the same cooling instability that has been previously discussed in the literature (e.g. Kafatos 1973; Gnat & Sternberg 2007; Oppenheimer & Schaye 2013; Vasiliev 2013), i.e. the gas cooling rate is faster than the recombination rate.

Given the Eulerian nature of the code, we cannot currently track the temperature and ionization history of individual gas parcels in the simulation¹⁸. It is important to note that at the current time, the cooling timescale does not need to be greater than the ionization timescale, rather, for an ionization lag to manifest, the cooling instability could have occurred any time in the very recent past.

We verified that the H II distribution exhibits the same out-of-equilibrium properties as the electron distribution, confirming that the source of the excess electrons are from H atoms. There are not enough metals for charge exchange reactions to push H II this far out of chemical equilibrium, ergo we conclude that catastrophic cooling is likely responsible for the gas that has strong non-equilibrium electron enhancements.

Figure 14 also shows that some gas has a non-equilibrium electron deficit compared to the equilibrium value (see also Richings & Schaye 2016). In these regions, the gas has been heated faster than it can be ionized. This gas tends to occupy much lower densities than the gas that is over-ionized compared to equilibrium. Strong shocks have been proposed as one mechanism to heat gas faster than it can be collisionally ionized (e.g. Klessen & Glover 2016). In our simulations, SN feedback in dense regions could be the source of

¹⁸ This will be remedied in future iterations of the PRISM model coupled to Monte Carlo tracer particles (Cadiou et al. 2019).

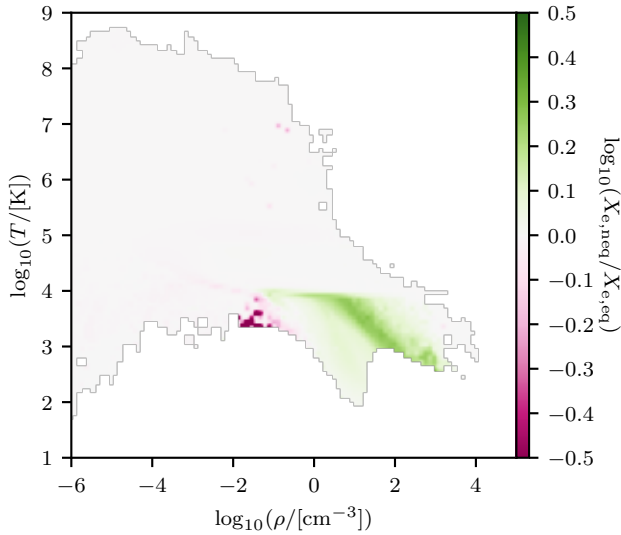


Figure 14. Logarithm of the ratio between the mass-weighted non-equilibrium and equilibrium electron fractions as a function of density and temperature in the G8 snapshot at 175 Myr. Gas is only shown if the electron fraction is at least 0.1%.

these shocks. However, here we propose that cosmic-ray heating might also cause this effect.

To demonstrate this, we have rerun our fiducial 1D model at $10^{-1} Z_{\odot}$ with $G_0 = 1$ and $\eta_{cr} = 10^{-16} \text{ s}^{-1} \text{ H}^{-1}$ generating a series of outputs between 0 and 20 Myr. In these simulations, we have initialized the gas temperature to 3 K. For each output, we then restart the calculation, fixing the temperature, and evolving the ionization states to equilibrium. In Figure 15 we show the gas temperature, non-equilibrium electron fraction, and ratio of non-equilibrium to equilibrium electron fraction as a function of density and time. At densities $> 10^2 \text{ cm}^{-3}$ the system is in chemical and thermal equilibrium beginning at timescales $\ll 1$ Myr. However, at low densities (i.e. $\rho < 10^{-1} \text{ cm}^{-3}$), the gas is significantly under-ionized, even at 20 Myr, when it is in thermal equilibrium. As we have shown in Figure 10, cosmic-ray heating dominates the heating rate at these densities in our simulation. We further demonstrate that this is the case in the 1D tests by showing the ratio of $\Gamma_{CR}/\Gamma_{Total}$ as a function of density and time. Indeed at these low densities, cosmic-rays account for nearly 100% of the total heating rate.

At intermediate densities (i.e. $10^0 < \rho/\text{cm}^{-3} < 10^2$), there is a transient effect where the gas can be over-ionized compared to equilibrium by $\sim 10\%$. This is not enough to account for the over-ionization observed in Figure 14, which exhibits values upwards of a factor of three. The origin of this effect also seems to be that cooling is faster than recombination. In the top row of Figure 15, at early times, the temperature over-shoots the equilibrium value. This overshoot allows the gas to be ionized above the equilibrium value (see second and third rows of Figure 15). As the gas cools down, the cooling timescale becomes shorter than the recombination timescale allowing for a small amount of over-ionization.

In summary, we have shown that there are regions of the ISM where, by mass, the electron fraction is both enhanced and reduced compared to equilibrium. This impacts not only the cooling and heating in the ISM, but also observable emission (Richings et al. 2022; Katz 2022). In future work, we will explore how star formation and line emission change due to non-equilibrium effects and more generally the PRISM model.

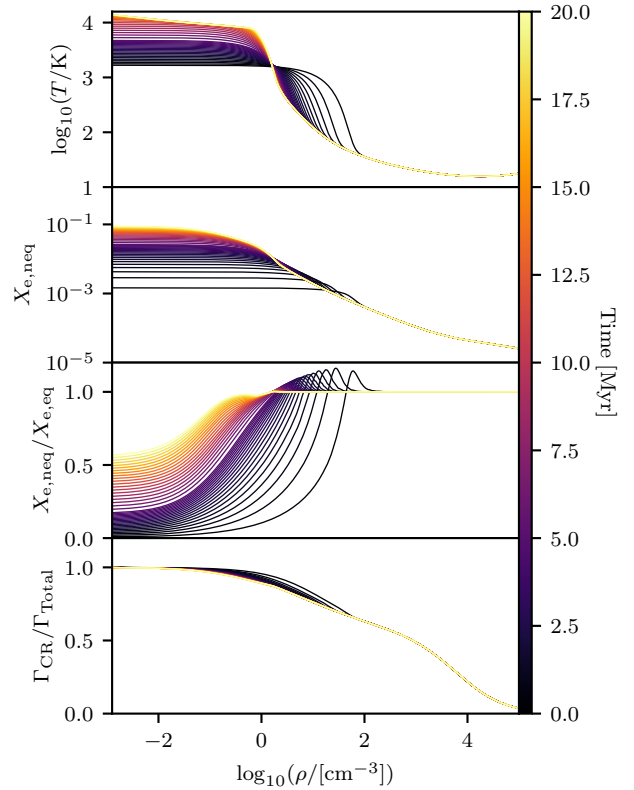


Figure 15. Gas temperature (first panel), non-equilibrium electron fraction (second panel), ratio of non-equilibrium to equilibrium electron fraction (third row), and ratio of cosmic-ray heating rate to the total heating rate (bottom panel) as a function of gas density for our fiducial 1D model at $10^{-1} Z_{\odot}$ with $G_0 = 1$ $\eta_{cr} = 10^{-16} \text{ s}^{-1} \text{ H}^{-1}$. Different colours represent different times as shown in the colour bar.

4 KNOWN LIMITATIONS AND FUTURE DEVELOPMENTS

Before proceeding to our conclusions, we highlight a few important limitations. As described above, we assume a dust-to-gas mass ratio based on oxygen abundance and a fixed dust composition. This assumption is unlikely to reflect the dust composition and abundance in all galactic environments and in some cases does not explicitly conserve mass. Furthermore, we apply a simplistic model for dust temperature. Future work that models dust production and destruction coupled to the radiation field in the context of RAMSES-RTZ and the PRISM model will ideally remedy these issues (Rodríguez Montero et al. *in prep*).

Thermal conduction is a potential important source of heat transport (Spitzer 1962) that is not included in our fiducial model. An accurate calculation of thermal conduction relies on properly modelling magnetic fields (which themselves can be an important pressure term in the ISM). We leave the inclusion of thermal conduction and magnetic fields to future work.

Our uniform model for cosmic-rays is unlikely to be an adequate representation of how cosmic-rays are actually distributed throughout galaxies. Current generations of simulations can now include cosmic-ray production, streaming, and diffusion, self-consistently (e.g. Chan et al. 2019; Farcy et al. 2022), and we anticipate a more accurate cosmic-ray implementation being an important future development for our model.

The cooling processes presented in this work are often only accu-

rate in the optically thin limit. This is especially true for our models of metal-line cooling and the exact density where the gas becomes optically thick depends on the specific transition. This can result in inaccuracies when the density of the gas goes above the critical density of the transition. For this reason, we recommend caution in applying our model in regimes that are not in the optically thin limit. Fortunately, densities of this magnitude are not typically reached by modern cosmological simulations; however, this may become problematic in giant molecular cloud simulations with sub-pc resolution aimed at modelling star formation.

Due to finite spatial and mass resolution, there is an upper limit on density that can be reached with simulations. This can impact the chemistry due to the n^2 -dependence of most of our chemical reactions. When important density structures are unresolved, our model may under-produce molecules such as CO and H₂ that tend to form at high densities. For this reason, we have adopted a sub-grid clumping factor, C , for H₂ formation, which impacts CO since CO formation is dependent on H₂ number density. Our fiducial model has $C = 1$, but depending on the simulation, this may need to be calibrated (Gnedin et al. 2009), e.g. on the observed H₂ column density distribution in the LMC or SMC (e.g. Tumlinson et al. 2002).

5 CONCLUSIONS

We have introduced the PRISM ISM model for thermochemistry and its coupling to the RAMSES-RTZ code. PRISM accounts for the dominant cooling and heating processes (i.e. photoheating, photoelectric heating, H₂ heating/cooling, cosmic-ray heating, primordial species cooling, metal-line cooling, CO cooling, and dust cooling) in the low-density ISM (i.e. $\rho \lesssim 10^5 \text{ cm}^{-3}$) as well as a non-equilibrium chemical network of up to 115 different species including the H₂ and CO molecules. All of these physical processes are fully coupled to the on-the-fly multifrequency radiation transport available in the RAMSES code (Teyssier 2002; Rosdahl et al. 2013). The combination of RAMSES-RTZ and PRISM is among the first suites of software to couple such a large chemical network to on-the-fly radiation hydrodynamics in an efficient enough manner to run full 3D cosmological (Katz et al. 2022) and isolated galaxy simulations (Cameron et al. 2022).

We have validated that PRISM model across six decades in metallicity by comparing with 1D equilibrium models in the literature (Koyama & Inutsuka 2000; Wolfire et al. 2003; Bialy & Sternberg 2019; Kim et al. 2022). We then applied the model to two isolated dwarf galaxy simulations (G8 and G9, similar in many respects to the SMC and LMC, Rosdahl et al. 2015) to take a census of which cooling and heating processes dominate different regions of a galaxy and to assess the importance of non-equilibrium effects. The 3D simulations differ in many ways from the 1D models due to the inclusion of ionizing radiation, a variable FUV radiation field, and self-shielding. This manifests in a much faster atomic-to-molecular transition in the simulations compared to the 1D models. Furthermore, we show that the electron fraction in the ISM can be more than three times enhanced or reduced in the ISM because of non-equilibrium effects (see also Richings & Schaye 2016). We attribute the enhancement to recombination lags where the cooling rate is faster than the recombination timescale. In contrast, we attribute electron fraction deficits to rapid cosmic-ray heating (in contrast to strong shocks), which is behaviour that can be reproduced in time-dependent 1D models.

Our presented model has known limitations. For example, we employ an effective model for dust, ignore magnetic fields and thermal conduction, do not self-consistently track cosmic-ray production and

transport, and the density squared dependence of many of the reactions leads to a resolution dependence in their abundance. In future work, we will develop the PRISM model to address these limitations in an effort to more accurately model the ISM and understand galaxy formation. The model is suitable for addressing numerous problems related to galaxy formation physics and the ISM. As a first application, it has recently been used to demonstrate the impact of temperature fluctuations of metallicity measurements (Cameron et al. 2022). Moving forward, we will extend our simulation suite to diverse environments from galaxy formation in a cosmological context to simulations of individual molecular clouds.

ACKNOWLEDGEMENTS

HK thanks Romain Teyssier for making the RAMSES code public. TK was supported by the National Research Foundation of Korea (NRF) grant funded by the Korea government (No. 2020R1C1C1007079 and No. 2022R1A6A1A03053472). MR is supported by the Beecroft Fellowship funded by Adrian Beecroft. OA and EA acknowledge financial support from the Knut and Alice Wallenberg Foundation and the Swedish Research Council (grant 2019-04659). This work was performed using the DiRAC Data Intensive service at Leicester, operated by the University of Leicester IT Services, which forms part of the STFC DiRAC HPC Facility. The equipment was funded by BEIS capital funding via STFC capital grants ST/K000373/1 and ST/R002363/1 and STFC DiRAC Operations grant ST/R001014/1. DiRAC is part of the National e-Infrastructure.

DATA AVAILABILITY

The data underlying this article will be shared on reasonable request to the corresponding author.

APPENDIX A: EQUILIBRIUM TEMPERATURE-DENSITY COMPARISON OF PRISM WITH Katz (2022) PHYSICS

In Figure A1 we compare the equilibrium temperature-density curves at various metallicities when using the fine-structure cooling collisional rates from Katz (2022) and not assuming the factor 1.5 increase in the photoelectric heating due to the updated PAH abundance as was done for our simulations. G8 and G9 were initialized at $0.1 Z_{\odot}$ and $0.5 Z_{\odot}$ and we see only small differences between the different models at $\rho \lesssim 10^3 \text{ cm}^{-3}$ for these metallicities. There is some difference at higher densities, primarily due to a change in the O I cooling. Our new model tabulates effective collision rates directly from CLOUDY (Ferland et al. 2017) for all fine-structure transitions in our model for the following collision partners: H, H⁺, ortho and para H₂, e⁻, He, He⁺, and He⁺⁺.

REFERENCES

- Agertz O., et al., 2021, *MNRAS*, **503**, 5826
- Andersson E. P., Agertz O., Renaud F., Teyssier R., 2022, arXiv e-prints, p. arXiv:2209.06218
- Anninos P., Zhang Y., Abel T., Norman M. L., 1997, *New Astron.*, **2**, 209
- Baczynski C., Glover S. C. O., Klessen R. S., 2015, *MNRAS*, **454**, 380
- Badnell N. R., 2006, *ApJS*, **167**, 334
- Badnell N. R., et al., 2003, *A&A*, **406**, 1151
- Bakes E. L. O., Tielens A. G. G. M., 1994, *ApJ*, **427**, 822
- Balashev S. A., et al., 2019, *MNRAS*, **490**, 2668

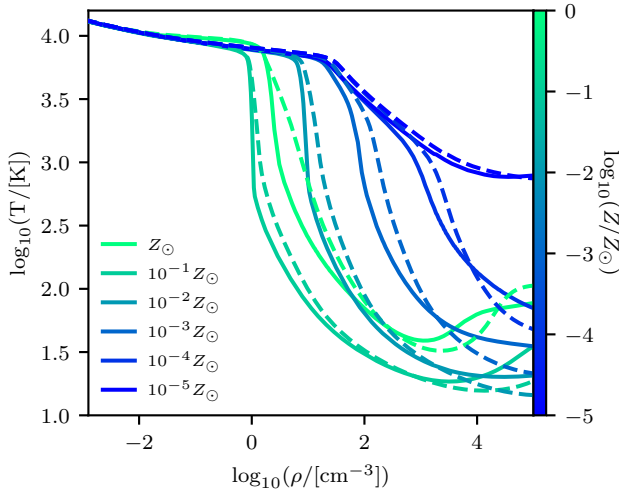


Figure A1. Equilibrium temperature-density relations as a function of metallicity. The solid lines show the fiducial PRISM model while the dashed lines represent the model using our previous fine-structure cooling collisional rates and not assuming the factor 1.5 boost in the photoelectric heating, as was done in [Katz \(2022\)](#). There are minimal differences between the two models with the previous model having slightly less efficient cooling.

Barrow K. S. S., Robertson B. E., Ellis R. S., Nakajima K., Saxena A., Stark D. P., Tang M., 2020, *ApJ*, **902**, L39
 Bialy S., Sternberg A., 2019, *ApJ*, **881**, 160
 Bieri R., Naab T., Geen S., Coles J. P., Pakmor R., Walch S., 2022, arXiv e-prints, p. [arXiv:2209.06842](#)
 Binette L., 1985, *A&A*, **143**, 334
 Black J. H., 1981, *MNRAS*, **197**, 553
 Black J. H., Dalgarno A., 1977, *ApJS*, **34**, 405
 Bolatto A. D., Wolfire M., Leroy A. K., 2013, *ARA&A*, **51**, 207
 Bovino S., Grassi T., Capelo P. R., Schleicher D. R. G., Banerjee R., 2016, *A&A*, **590**, A15
 Buck T., Pfrommer C., Girichidis P., Corobean B., 2022, *MNRAS*, **513**, 1414
 Burton M. G., Hollenbach D. J., Tielens A. G. G. M., 1990, *ApJ*, **365**, 620
 Cadiou C., Dubois Y., Pichon C., 2019, *A&A*, **621**, A96
 Cameron A. J., Katz H., Rey M. P., 2022, arXiv e-prints, p. [arXiv:2210.14234](#)
 Cen R., 1992, *ApJS*, **78**, 341
 Chan T. K., Kereš D., Hopkins P. F., Quataert E., Su K. Y., Hayward C. C., Faucher-Giguère C. A., 2019, *MNRAS*, **488**, 3716
 Christensen C., Quinn T., Governato F., Stille A., Shen S., Wadsley J., 2012, *MNRAS*, **425**, 3058
 Cox D. P., Smith B. W., 1974, *ApJ*, **189**, L105
 Crenny T., Federman S. R., 2004, *ApJ*, **605**, 278
 Dalgarno A., McCray R. A., 1972, *ARA&A*, **10**, 375
 Dopita M. A., Kewley L. J., Heisler C. A., Sutherland R. S., 2000, *ApJ*, **542**, 224
 Draine B. T., 2011, *Physics of the Interstellar and Intergalactic Medium*
 Draine B. T., Bertoldi F., 1996, *ApJ*, **468**, 269
 Draine B. T., Sutin B., 1987, *ApJ*, **320**, 803
 Dubois Y., et al., 2014, *MNRAS*, **444**, 1453
 Farcy M., Rosdahl J., Dubois Y., Blaizot J., Martin-Alvarez S., 2022, *MNRAS*, **513**, 5000
 Federman S. R., Huntress W. T. J., Prasad S. S., 1990, *ApJ*, **354**, 504
 Federrath C., Klessen R. S., 2012, *ApJ*, **761**, 156
 Ferland G. J., Korista K. T., Verner D. A., Ferguson J. W., Kingdon J. B., Verner E. M., 1998, *PASP*, **110**, 761
 Ferland G. J., et al., 2017, *Rev. Mex. Astron. Astrofis.*, **53**, 385
 Field G. B., Goldsmith D. W., Habing H. J., 1969, *ApJ*, **155**, L149
 Galli D., Palla F., 1998, *A&A*, **335**, 403
 Gerin M., et al., 2015, *A&A*, **573**, A30

Girichidis P., et al., 2016, *ApJ*, **816**, L19
 Glover S. C. O., Clark P. C., 2012a, *MNRAS*, **421**, 116
 Glover S. C. O., Clark P. C., 2012b, *MNRAS*, **426**, 377
 Glover S. C. O., Federrath C., Mac Low M. M., Klessen R. S., 2010, *MNRAS*, **404**, 2
 Gnat O., Sternberg A., 2007, *ApJS*, **168**, 213
 Gnedin N. Y., Tassis K., Kravtsov A. V., 2009, *ApJ*, **697**, 55
 Goldsmith D. W., Habing H. J., Field G. B., 1969, *ApJ*, **158**, 173
 Gong M., Ostriker E. C., Kim C.-G., Kim J.-G., 2020, *ApJ*, **903**, 142
 Gray W. J., Scannapieco E., Kasen D., 2015, *ApJ*, **801**, 107
 Gredel R., Lepp S., Dalgarno A., 1987, *ApJ*, **323**, L137
 Gredel R., Lepp S., Dalgarno A., Herbst E., 1989, *ApJ*, **347**, 289
 Grevesse N., Asplund M., Sauval A. J., Scott P., 2010, *Ap&SS*, **328**, 179
 Gutcke T. A., Pakmor R., Naab T., Springel V., 2021, *MNRAS*, **501**, 5597
 Haardt F., Madau P., 2012, *ApJ*, **746**, 125
 Habing H. J., 1968, *Bull. Astron. Inst. Netherlands*, **19**, 421
 Haiman Z., Thoul A. A., Loeb A., 1996, *ApJ*, **464**, 523
 Heays A. N., Bosman A. D., van Dishoeck E. F., 2017, *A&A*, **602**, A105
 Heger A., Woosley S. E., 2002, *ApJ*, **567**, 532
 Herrera-Camus R., et al., 2017, *ApJ*, **835**, 201
 Hill A. S., Mac Low M.-M., Gatto A., Ibáñez-Mejía J. C., 2018, *ApJ*, **862**, 55
 Hjellming R. M., 1966, *ApJ*, **143**, 420
 Hollenbach D., McKee C. F., 1979, *ApJS*, **41**, 555
 Hollenbach D., McKee C. F., 1989, *ApJ*, **342**, 306
 Hopkins P. F., et al., 2018, *MNRAS*, **480**, 800
 Hu C.-Y., Sternberg A., van Dishoeck E. F., 2021, *ApJ*, **920**, 44
 Hui L., Gnedin N. Y., 1997, *MNRAS*, **292**, 27
 Hummels C. B., et al., 2019, *ApJ*, **882**, 156
 Iffrig O., Hennebelle P., 2017, *A&A*, **604**, A70
 Indriolo N., McCall B. J., 2012, *ApJ*, **745**, 91
 Jenkins E. B., Tripp T. M., 2011, *ApJ*, **734**, 65
 Kafatos M., 1973, *ApJ*, **182**, 433
 Kannan R., Marinacci F., Vogelsberger M., Sales L. V., Torrey P., Springel V., Hernquist L., 2020, *MNRAS*, **499**, 5732
 Katz H., 2022, *MNRAS*, **512**, 348
 Katz H., Kimm T., Sijacki D., Haehnelt M. G., 2017, *MNRAS*, **468**, 4831
 Katz H., et al., 2019, *MNRAS*, **487**, 5902
 Katz H., Kimm T., Ellis R. S., Devriendt J., Slyz A., 2022, arXiv e-prints, p. [arXiv:2207.04751](#)
 Kewley L. J., Dopita M. A., Sutherland R. S., Heisler C. A., Trevena J., 2001, *ApJ*, **556**, 121
 Kim C.-G., Ostriker E. C., 2017, *ApJ*, **846**, 133
 Kim C.-G., et al., 2020, *ApJ*, **900**, 61
 Kim J.-G., Gong M., Kim C.-G., Ostriker E. C., 2022, arXiv e-prints, p. [arXiv:2210.08024](#)
 Kimm T., Cen R., Devriendt J., Dubois Y., Slyz A., 2015, *MNRAS*, **451**, 2900
 Kimm T., Katz H., Haehnelt M., Rosdahl J., Devriendt J., Slyz A., 2017, *MNRAS*, **466**, 4826
 Kimm T., Haehnelt M., Blaizot J., Katz H., Michel-Dansac L., Garel T., Rosdahl J., Teyssier R., 2018, *MNRAS*, **475**, 4617
 Kingdon J. B., Ferland G. J., 1996, *ApJS*, **106**, 205
 Klessen R. S., Glover S. C. O., 2016, *Saas-Fee Advanced Course*, **43**, 85
 Klimenko V. V., Balashev S. A., 2020, *MNRAS*, **498**, 1531
 Koyama H., Inutsuka S.-I., 2000, *ApJ*, **532**, 980
 Langer W. D., 1978, *ApJ*, **225**, 860
 Leboutteiller V., Ramambason L., 2022, arXiv e-prints, p. [arXiv:2207.05657](#)
 Lee H. H., Herbst E., Pineau des Forets G., Roueff E., Le Bourlot J., 1996, *A&A*, **311**, 690
 Lepp S., Shull J. M., 1984, *ApJ*, **280**, 465
 Levermore C. D., 1984, *J. Quant. Spectrosc. Radiative Transfer*, **31**, 149
 Liu Y., Kretschmer M., Teyssier R., 2022, *MNRAS*, **513**, 6028
 Lotz W., 1967, *ApJS*, **14**, 207
 Lupi A., Pallottini A., Ferrara A., Bovino S., Carniani S., Vallini L., 2020, *MNRAS*, **496**, S160
 Mandelker N., van den Bosch F. C., Springel V., van de Voort F., Burchett J. N., Butsky I. S., Nagai D., Oh S. P., 2021, *ApJ*, **923**, 115
 McCourt M., Oh S. P., O'Leary R., Madigan A.-M., 2018, *MNRAS*, **473**, 5407

- McKee C. F., Ostriker J. P., 1977, *ApJ*, **218**, 148
- McKee C. F., Storey J. W. V., Watson D. M., Green S., 1982, *ApJ*, **259**, 647
- Morisset C., Delgado-Inglada G., Flores-Fajardo N., 2015, *Rev. Mex. Astron. Astrofis.*, **51**, 103
- Nelson R. P., Langer W. D., 1997, *ApJ*, **482**, 796
- Neufeld D. A., Lepp S., Melnick G. J., 1995, *ApJS*, **100**, 132
- Nomoto K., Tominaga N., Umeda H., Kobayashi C., Maeda K., 2006, *Nuclear Phys. A*, **777**, 424
- Norman C. A., Spaans M., 1997, *ApJ*, **480**, 145
- Olsen K., et al., 2018, *Galaxies*, **6**, 100
- Omukai K., 2000, *ApJ*, **534**, 809
- Omukai K., Tsuribe T., Schneider R., Ferrara A., 2005, *ApJ*, **626**, 627
- Oppenheimer B. D., Schaye J., 2013, *MNRAS*, **434**, 1043
- Oppenheimer B. D., Schaye J., Crain R. A., Werk J. K., Richings A. J., 2018, *MNRAS*, **481**, 835
- Osterbrock D. E., Ferland G. J., 2006, *Astrophysics of gaseous nebulae and active galactic nuclei*
- Pallottini A., et al., 2022, *MNRAS*, **513**, 5621
- Peeples M. S., et al., 2019, *ApJ*, **873**, 129
- Peters T., et al., 2017, *MNRAS*, **466**, 3293
- Pignatari M., et al., 2016, *ApJS*, **225**, 24
- Portinari L., Chiosi C., Bressan A., 1998, *A&A*, **334**, 505
- Rachford B. L., et al., 2002, *ApJ*, **577**, 221
- R  my-Ruyer A., et al., 2014, *A&A*, **563**, A31
- Rey M. P., Pontzen A., Agertz O., Orkney M. D. A., Read J. I., Saintonge A., Pedersen C., 2019, *ApJ*, **886**, L3
- Richings A. J., Schaye J., 2016, *MNRAS*, **458**, 270
- Richings A. J., Schaye J., Oppenheimer B. D., 2014, *MNRAS*, **440**, 3349
- Richings A. J., Faucher-Gigu  re C.-A., Gurvich A. B., Schaye J., Hayward C. C., 2022, arXiv e-prints, p. [arXiv:2208.02288](https://arxiv.org/abs/2208.02288)
- Riechers D. A., et al., 2019, *ApJ*, **872**, 7
- R  llig M., Ossenkopf V., Jeyakumar S., Stutzki J., Sternberg A., 2006, *A&A*, **451**, 917
- Rosdahl J., Blaizot J., Aubert D., Stranex T., Teyssier R., 2013, *MNRAS*, **436**, 2188
- Rosdahl J., Schaye J., Teyssier R., Agertz O., 2015, *MNRAS*, **451**, 34
- Rosdahl J., et al., 2018, *MNRAS*, **479**, 994
- Saslaw W. C., Zipoy D., 1967, *Nature*, **216**, 976
- Schaye J., et al., 2015, *MNRAS*, **446**, 521
- Seitenzahl I. R., et al., 2013, *MNRAS*, **429**, 1156
- Sheffer Y., Rogers M., Federman S. R., Abel N. P., Gredel R., Lambert D. L., Shaw G., 2008, *ApJ*, **687**, 1075
- Silk J., 1970, *Astrophys. Lett.*, **5**, 283
- Smith B. D., et al., 2017, *MNRAS*, **466**, 2217
- Solomon P. M., Klemperer W., 1972, *ApJ*, **178**, 389
- Sparre M., Pfrommer C., Vogelsberger M., 2019, *MNRAS*, **482**, 5401
- Spitzer L., 1962, *Physics of Fully Ionized Gases*
- Stanway E. R., Eldridge J. J., 2018, *MNRAS*, **479**, 75
- Sternberg A., Dalgarno A., 1989, *ApJ*, **338**, 197
- Sternberg A., Le Petit F., Roueff E., Le Bourlot J., 2014, *ApJ*, **790**, 10
- Sutherland R. S., Dopita M. A., 1993, *ApJS*, **88**, 253
- Teyssier R., 2002, *A&A*, **385**, 337
- Tielens A. G. G. M., Hony S., van Kerckhoven C., Peeters E., 1999, in Cox P., Kessler M., eds, *ESA Special Publication Vol. 427, The Universe as Seen by ISO*. p. 579
- Tumlinson J., et al., 2002, *ApJ*, **566**, 857
- Turk M. J., Clark P., Glover S. C. O., Greif T. H., Abel T., Klessen R., Bromm V., 2011, *ApJ*, **726**, 55
- Vasiliev E. O., 2013, *MNRAS*, **431**, 638
- Verner D. A., Ferland G. J., Korista K. T., Yakovlev D. G., 1996, *ApJ*, **465**, 487
- Vogelsberger M., et al., 2014, *MNRAS*, **444**, 1518
- Voronov G. S., 1997, *Atomic Data and Nuclear Data Tables*, **65**, 1
- Walch S., et al., 2015, *MNRAS*, **454**, 238
- Weingartner J. C., Draine B. T., 2001, *ApJ*, **563**, 842
- Welty D. E., Lauroesch J. T., Wong T., York D. G., 2016, *ApJ*, **821**, 118
- Wiersma R. P. C., Schaye J., Smith B. D., 2009, *MNRAS*, **393**, 99
- Williams R. E., 1967, *ApJ*, **147**, 556
- Wolfire M. G., Hollenbach D., McKee C. F., Tielens A. G. G. M., Bakes E. L. O., 1995, *ApJ*, **443**, 152
- Wolfire M. G., McKee C. F., Hollenbach D., Tielens A. G. G. M., 2003, *ApJ*, **587**, 278
- Wolfire M. G., Tielens A. G. G. M., Hollenbach D., Kaufman M. J., 2008, *ApJ*, **680**, 384
- Yoneyama T., 1972, *PASJ*, **24**, 87
- Zubko V., Dwek E., Arendt R. G., 2004, *ApJS*, **152**, 211

This paper has been typeset from a \LaTeX file prepared by the author.